Cell Stem Cell

Article

Dissecting the molecular basis of human interneuron migration in forebrain assembloids from Timothy syndrome

Graphical abstract

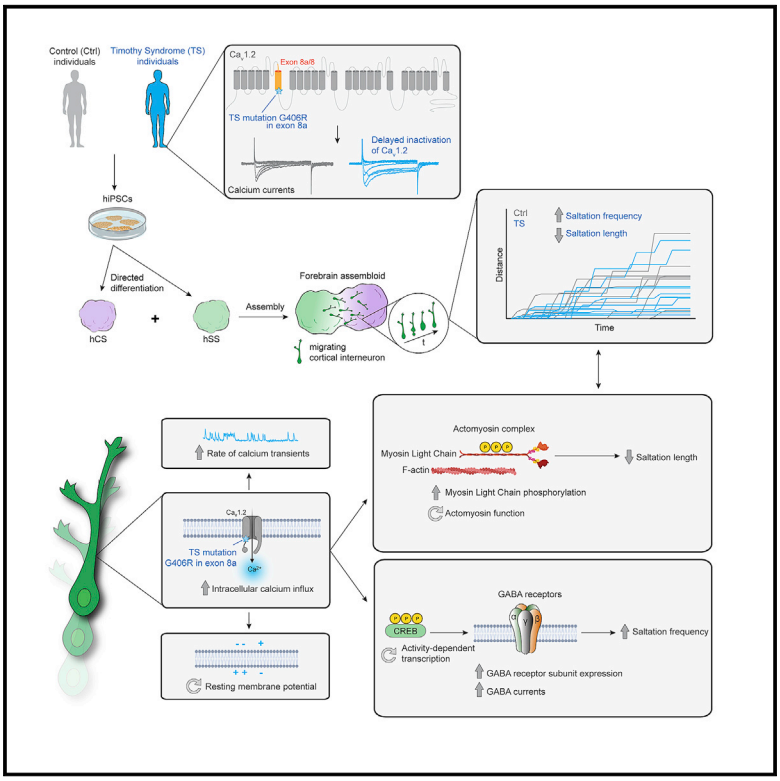

Highlights

- TS interneurons display soma rear-front uncoupling in forebrain assembloids
- Aberrant actomyosin function leads to decreased saltation length in TS interneurons
- Changes in GABA sensitivity modulate saltation frequency in TS interneurons
- Abnormal hCS network activity in TS is exacerbated by migrated interneurons

Authors

Fikri Birey, Min-Yin Li, Aaron Gordon, ..., Anca M. Paşca, Daniel H. Geschwind, Sergiu P. Paşca

Correspondence

spasca@stanford.edu

In brief

Using forebrain assembloids, Birey et al. describe the molecular mechanisms underlying the cell-autonomous migration defect in human cortical interneurons derived from individuals with Timothy syndrome. These findings provide novel, cell-type-specific insights into L-type calcium channel-mediated modulation of cortical development.

Birey et al., 2022, Cell Stem Cell *29*, 1–17
February 3, 2022
https://doi.org/10.1016/j.stem.2021.11.011

CellPress

Cell Stem Cell

CellPress

Article

Dissecting the molecular basis of human interneuron migration in forebrain assembloids from Timothy syndrome

Fikri Birey,[1,2] Min-Yin Li,[1,2] Aaron Gordon,[3] Mayuri V. Thete,[1,2] Alfredo M. Valencia,[1,2] Omer Revah,[1,2] Anca M. Paşca,[4,7] Daniel H. Geschwind,[3,4,5,6] and Sergiu P. Paşca[1,2,8,*]

[1]Department of Psychiatry and Behavioral Sciences, Stanford University School of Medicine, Stanford, CA 94305, USA
[2]Stanford Brain Organogenesis, Wu Tsai Neurosciences Institute, Stanford University, Stanford, CA 94305, USA
[3]Program in Neurogenetics, Department of Neurology, University of California, Los Angeles, Los Angeles, CA 90095, USA
[4]Department of Human Genetics, David Geffen School of Medicine, University of California, Los Angeles, Los Angeles, CA 90095, USA
[5]Center for Autism Research and Treatment, Semel Institute, University of California, Los Angeles, Los Angeles, CA 90095, USA
[6]Institute of Precision Health, University of California, Los Angeles, Los Angeles, CA 90095, USA
[7]Department of Pediatrics, Division of Neonatology, Stanford University, Stanford, CA 94305, USA
[8]Lead contact
*Correspondence: spasca@stanford.edu
https://doi.org/10.1016/j.stem.2021.11.011

SUMMARY

Defects in interneuron migration can disrupt the assembly of cortical circuits and lead to neuropsychiatric disease. Using forebrain assembloids derived by integration of cortical and ventral forebrain organoids, we have previously discovered a cortical interneuron migration defect in Timothy syndrome (TS), a severe neurodevelopmental disease caused by a mutation in the L-type calcium channel (LTCC) $Ca_v1.2$. Here, we find that acute pharmacological modulation of $Ca_v1.2$ can regulate the saltation length, but not the frequency, of interneuron migration in TS. Interestingly, the defect in saltation length is related to aberrant actomyosin and myosin light chain (MLC) phosphorylation, while the defect in saltation frequency is driven by enhanced γ-aminobutyric acid (GABA) sensitivity and can be restored by GABA-A receptor antagonism. Finally, we describe hypersynchronous hCS network activity in TS that is exacerbated by interneuron migration. Taken together, these studies reveal a complex role of LTCC function in human cortical interneuron migration and strategies to restore deficits in the context of disease.

INTRODUCTION

The formation of the cerebral cortex involves the assembly of glutamatergic neurons and GABAergic interneurons into circuits during fetal development (Silva et al., 2019). Glutamatergic neurons are generated in the dorsal forebrain, whereas GABAergic interneurons are generated in the ventral forebrain, and undergo extensive tangential migration to reach the cerebral cortex (Anderson et al., 1997; Marín, 2013; Wamsley and Fishell, 2017). Migration of cortical interneurons has been investigated in rodents, and it involves motion of a leading branch that subsequently gets stabilized in the direction of forward movement; this triggers various cytoskeletal rearrangements that create a pulling force at the leading branch and a pushing force at the cell rear. This process leads to what is referred to as nucleokinesis and underlies the saltatory mode of migration of cortical interneurons (Schaar and McConnell, 2005; Bellion et al., 2005; Martini and Valdeolmillos, 2010).

The migration of human cortical interneurons spans a significant fraction of *in utero* development and, unlike in rodents (Inamura et al., 2012), continues after birth in humans (Silbereis et al., 2016). Genetic perturbations that affect this process are thought to lead to miswiring of cortical circuits and contribute to disease, including schizophrenia (SCZ), autism spectrum disorder (ASD), and epilepsy (Meechan et al., 2012; Powell, 2013; Muraki and Tanigaki, 2015; Buchsbaum and Cappello, 2019; Maset et al., 2021). However, how these genetic, disease-related events impact neuronal migration and cortical circuit assembly in humans remains elusive, mainly due to the lack of brain tissue from patients for functional studies. To start addressing this limitation, we have previously developed forebrain assembloids (Birey et al., 2017)—a 3D *in vitro* platform in which region-specific forebrain organoids or spheroids derived from human-induced pluripotent stem cells (hiPSCs) are physically and functionally integrated. We used this system to model the migration of human cortical interneurons into glutamatergic neuronal networks and demonstrated that their migration kinetics were reminiscent of GABAergic neurons in *ex vivo* human forebrain specimens.

Cortical interneuron migration has been previously shown to be dependent on L-type calcium channel (LTCC) function (Bortone and Polleux, 2009; Kamijo et al., 2018), and genetic variants that alter LTCC function have been implicated in various

Please cite this article in press as: Birey et al., Dissecting the molecular basis of human interneuron migration in forebrain assembloids from Timothy syndrome, Cell Stem Cell (2021), https://doi.org/10.1016/j.stem.2021.11.011

neuropsychiatric disorders (Bhat et al., 2012; Purcell et al., 2014; Ripke et al., 2014). For instance, gain-of-function mutations in the *CACNA1C* gene, which encodes the pore-forming subunit of $Ca_v1.2$, cause Timothy syndrome (TS)—a rare and highly penetrant neurodevelopmental disorder (NDD) associated with ASD and epilepsy (Splawski et al., 2004). Using forebrain assembloids derived from patients with TS, we have previously uncovered a migration phenotype in TS interneurons in which the saltation length was reduced, but the saltation frequency was increased; overall leading to inefficient migration (Birey et al., 2017). However, the molecular mechanisms underlying the compound nature of this migration defect have been unknown.

Here, we investigate the molecular basis of the TS migration defect using calcium imaging, long-term live cell imaging, pharmacology, whole-cell patch clamping, and RNA sequencing in forebrain assembloids and *ex vivo* primary human cortical slice cultures. We discover that defects in TS interneuron saltation length and frequency are driven by distinct molecular pathways, elucidating a unique mode of LTCC-mediated regulation of human cortical interneuron migration in the context of disease.

RESULTS

Uncoupling of cell rear-front coordination in migrating TS cortical interneurons

To investigate the molecular basis of the human cortical interneuron migration deficits in TS, we assembled human cortical spheroids (hCSs) and human subpallial spheroids (hSSs) to generate forebrain assembloids from hiPSCs derived from 8 control (Ctrl) individuals and 3 individuals with TS carrying the G406R mutation in the alternatively spliced exon 8a of *CACNA1C* (Splawski et al., 2004) (Figures 1A and 1B; Table S1 summarizes the use of hiPSC lines in various experiments). The point mutation leads to delayed inactivation of the $Ca_v1.2$ channel and increased intracellular calcium entry (Figures 1B and 1C). To visualize interneurons in forebrain assembloids, we used a lentiviral reporter for the interneuron lineage (Dlxi1/2b-eGFP or Dlxi1/2b-mScarlet). $Ca_v1.2$ was abundantly expressed in Dlxi1/2b$^+$ human neurons (Figure S1A). G406R-containing exon 8a isoform is the dominant isoform present during development, which is replaced in relative abundance by exon 8 isoform in the postnatal cerebral cortex (Panagiotakos et al., 2019). Because of aberrant splicing caused by G406R mutation, the developmental switch from exon 8a to exon 8 isoform is hindered in TS, prolonging the enrichment of the TS mutation-containing 8a isoform at later time points in hCS (Figure S1B), hSS (Figure S1C), as well as Dlxi1/2b-eGFP$^+$ interneurons isolated from forebrain assembloids (Figures S1D and S1E), consistent with previous studies (Paşca et al., 2011; Panagiotakos et al., 2019).

We have previously found that TS interneurons migrate inefficiently (Figure 1D, $p < 0.0001$, two-way ANOVA for Ctrl versus TS) because of a reduction in the distance of individual saltations (“saltation length”) concomitant with an increase in the number of saltations (“saltation frequency”) (Figure 1E; Birey et al., 2017). $Ca_v1.2$ activity is modulated by several classes of drugs. Interestingly, we found that the 1,4-dihydropyridine LTCC blocker nimodipine (Nim, 5 μM) increased the saltation length but did not affect the saltation frequency, suggesting that the two phenotypes might be driven by distinct molecular pathways (Figure 1E, Ctrl saltation length: $p < 0.0001$; TS saltation length: $p < 0.0001$). Another dihydropyridine LTCC blocker, isradipine (3 μM), also increased the saltation length although it reduced the saltation frequency (Figure S1F); this could be due to differences in dose and effect of isradipine on other LTCCs.

A quantitative understanding of interneuron migration dynamics is limited by the lack of tools to precisely track multiple, simultaneously moving cellular compartments over long periods of time. To overcome this issue, we performed fast, high-resolution imaging of migrating cortical interneurons and applied a transfer learning-based pose estimation algorithm called DeepLabCut (Mathis et al., 2018) to extract subcellular features associated with TS interneuron migration. Used for marker-less pose estimation of user-defined body parts in animal behavioral studies (Mathis and Mathis, 2020), DeepLabCut uses a small number of training frames (19), with which the user manually defines regions of interests (ROIs) to be tracked. We reasoned that this method could be used to train a network to track discrete subcellular ROIs during interneuron migration without the need for localized fluorescent reporters (Figure 1F; Video S1). Indeed, we verified that the pipeline could detect a reduction in the saltation length in TS (Figure S1G, soma front: $p < 0.0001$; soma rear: $p < 0.0001$). Previous work has extensively characterized the functional polarization of the migration machinery in cortical interneurons, with microtubules in the leading branch and the actomyosin network in the soma rear, which mediate pulling and pushing forces during nucleokinesis, respectively (Bellion et al., 2005). To estimate the contribution of pulling versus pushing forces during nucleokinesis in Ctrl and TS interneurons, we focused on independently monitoring soma rear and front. This analysis revealed an uncoupling of soma rear-front coordination in TS interneurons; while soma rear and front moved in synchrony during Ctrl interneuron saltations, the rear appeared uncoupled from the front of the soma during TS interneuron saltations (Figures 1G and 1H; Video S2). More specifically, the soma rear lagged behind the soma front in the course of a saltation, which was quantified by calculating the correlation coefficient between soma front and soma rear movements (Figure 1I, $p < 0.001$). To validate this phenotype using an orthogonal approach, we performed high-resolution imaging of migrating Dlxi1/2b-eGFP$^+$ interneurons in the hCS side of assembloid cryosections. We reasoned that, because nucleokinesis events are prolonged in TS interneurons due to rear/front uncoupling (Figures 1G and 1H), we are prone to identify more Dlx1/2b-GFP$^+$ somas that are elongated in TS (due to the rear pushing being delayed) compared to Ctrl (where the rear/front movement is well-coordinated). To our knowledge, there are no reliable markers to specifically delineate soma front and rear, so we morphologically identified interneurons that were in a “pre-saltation state" characterized by proximal leading branch thinning and distal leading branch swelling. The soma rear was defined at the rear-most part of the soma and the soma front was defined at the thinnest part of the proximal leading branch. Using these landmarks, we isolated the soma from Ctrl and TS interneurons that were in the pre-saltation state, 3D-rendered the volume images and calculated their

Please cite this article in press as: Birey et al., Dissecting the molecular basis of human interneuron migration in forebrain assembloids from Timothy syndrome, Cell Stem Cell (2021), https://doi.org/10.1016/j.stem.2021.11.011

CellPress

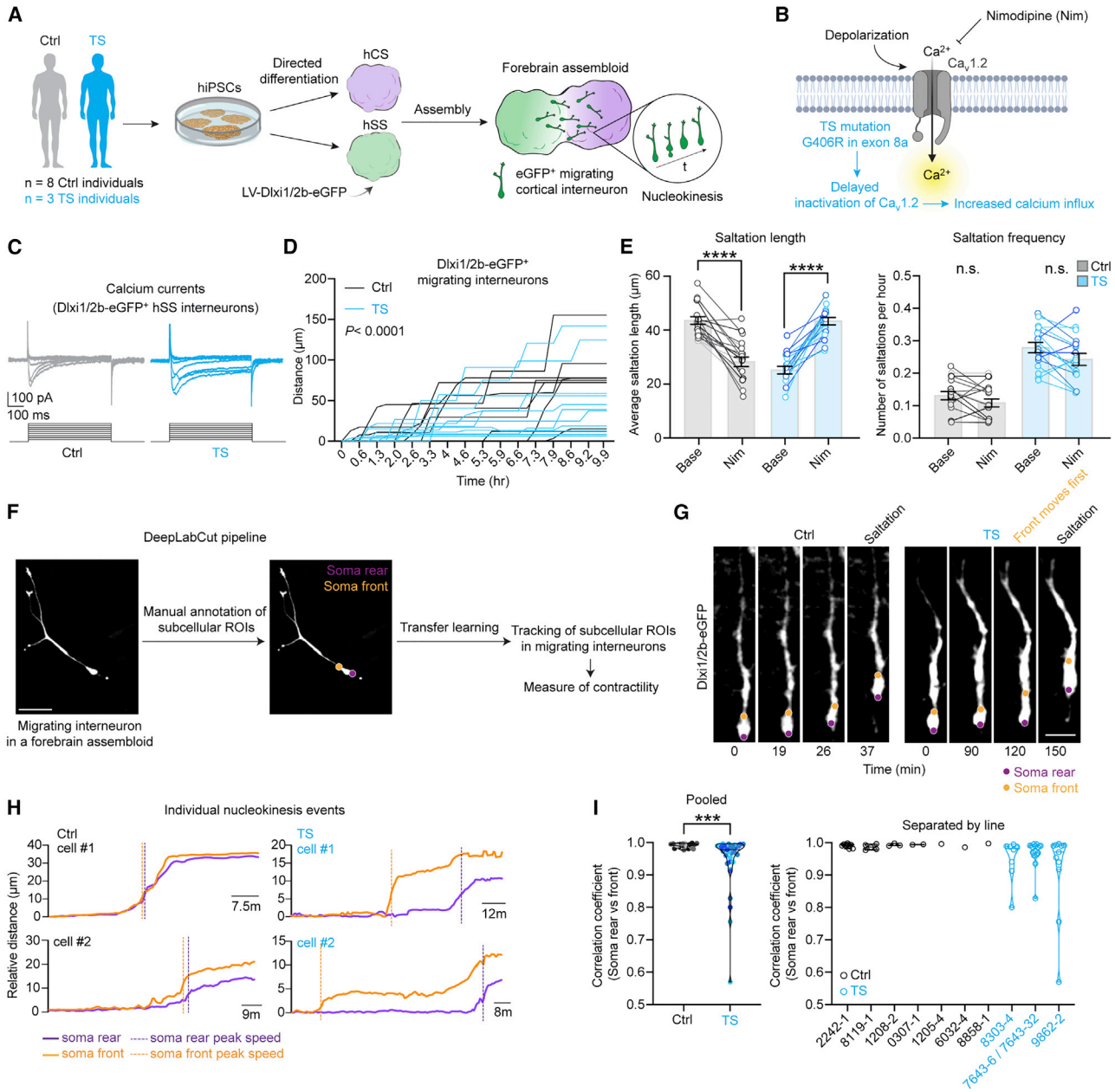

Figure 1. Uncoupling of soma rear-front coordination during nucleokinesis in TS interneurons

(A) Schematic illustrating the generation of forebrain assembloids by integrating hCS and hSS from hiPSCs derived from 8 Ctrl individuals and 3 individuals with TS.

(B) Schematic illustrating the impact of TS mutation G406R on $Ca_v1.2$ function.

(C) Calcium currents recorded from monolayer hSS neurons (day 144) labeled with Dlxi1/2b-eGFP.

(D) Distance versus time plots demonstrating inefficient migration of TS interneurons (Ctrl, n = 9 cells from 2 hiPSC lines, 1 assembloid per line; TS, n = 11 cells from 2 hiPSC lines, 1 assembloid per line. Two-way ANOVA for subjects, $F_{18,540} = 48.59$, ****$p < 0.0001$).

(E) The effect of Nimodipine (Nim) on the saltation length and frequency phenotypes in TS interneurons (Ctrl, n = 19 cells from 4 hiPSC lines, 1–4 assembloid per line; TS, n = 17 cells from 3 hiPSC lines, 2–3 assembloids per line. Paired t test, ****$p < 0.0001$).

(F) Schematic illustrating the DeepLabCut analysis pipeline.

(G) Representative live migration imaging snapshots of a migrating Ctrl and TS interneuron where soma rear and front positions were tracked using DeepLabCut.

(H) Distance versus time plots of individual saltation events demonstrating soma rear-front uncoupling in TS interneurons.

(I) Quantification of correlation coefficient (Pearson's R) between soma rear and soma front per saltation event (left: pooled, right: separated by line. Ctrl, n = 23 cells from 7 hiPSC lines, 1–4 assembloid per line; TS, n = 32 cells from 3 hiPSC lines, 1–5 assembloid per line. Mann-Whitney test, ***$p < 0.001$). Bar charts: mean ± SEM, violin plots: center line, median. Scale bars: 40 μm in (F) and 10 μm in (G). n.s., not significant. For (E and I), different shades of gray represent individual Ctrl hiPSC lines. Different shades of cyan represent individual TS hiPSC lines.

Please cite this article in press as: Birey et al., Dissecting the molecular basis of human interneuron migration in forebrain assembloids from Timothy syndrome, Cell Stem Cell (2021), https://doi.org/10.1016/j.stem.2021.11.011

sphericity. We also performed the same analysis with DAPI$^+$ nuclei from the same cells. This analysis showed reduced sphericity of TS soma ($p < 0.01$) and nuclei ($p < 0.05$), providing further support for impaired nucleokinesis by incoordination between the rear and front in TS (Figures S1H–S1J). Overall, these results indicated that cell-rear contractility may be selectively disrupted in migrating TS interneurons.

Acute modulation of LTCCs and intracellular calcium affect saltation length, but not saltation frequency, in TS forebrain assembloids and *ex vivo* forebrain tissue

Contractility in cells and tissues, such as skeletal muscle cells (Kuo and Ehrlich, 2015), is a calcium-dependent process (Bers, 2002). Given the cell-rear contractility deficits in TS, where the G406R mutation leads to increased intracellular calcium ($[Ca^{2+}]_i$), we asked which aspects of the phenotype are calcium-dependent (Figure 2A), as opposed to calcium-independent mechanisms underlying dendrite retraction in TS cortical glutamatergic neurons (Krey et al., 2013). We performed live imaging in forebrain assembloids in a medium with modified extracellular concentrations of calcium ($[Ca^{2+}]_e$) (Figures 2B and S2A) and found that compared with baseline levels (2 mM $[Ca^{2+}]_e$), a reduction to 0.5 mM $[Ca^{2+}]_e$ severely impacted interneuron migration bringing most cells to a stop in both genotypes (Figure S2B). Migration in 1 mM $[Ca^{2+}]_e$ was not as severely affected, with 63% and 27% of migrating interneurons coming to a stop in Ctrl and TS interneurons, respectively (Figure 2C, $p < 0.01$). Interestingly, out of the cells that performed at least one saltation in 1 mM $[Ca^{2+}]_e$ (“mobile cells”), we found that the saltation length in TS interneurons was partially restored, while the saltation length in Ctrl interneurons was reduced, suggesting that the TS saltation length phenotype is calcium-dependent. Saltation frequency was significantly reduced in both groups likely due to intolerance to longer exposure to less than 2 mM $[Ca^{2+}]_e$ (Figure 2D, Ctrl saltation length: $p < 0.05$; TS saltation length: $p < 0.01$; Ctrl saltation frequency: $p < 0.01$; TS saltation frequency: $p < 0.0001$).

To validate the effect of the acute modulation of LTCCs and $[Ca^{2+}]_i$ levels on the saltation length phenotype in an *ex vivo* preparation, we prepared primary human cortical slices at 18 postconceptional weeks (PCW18). We labeled interneurons with the same lentiviral reporter used for assembloid migration imaging (Dlxi1/2b-eGFP) and then performed migration imaging in slices in the presence of a potent non-dihydropyridine LTCC activator, FPL 64176 (5 μM, Figures 2E and 2F). While FPL 64176 application reduced the saltation length of migrating primary cortical interneurons, it had no effect on their saltation frequency, supporting the view that LTCC-mediated calcium influx acutely modulates saltation length but not the saltation frequency of migrating cortical interneurons (Figure 2G, saltation length: $p < 0.0001$). We also performed 2-day-long imaging without any drug application and asked whether the imaging paradigm itself influenced primary cortical interneuron migration (Figures S2C and S2D), which revealed no changes in the migration kinetics. Because both activation and inhibition of LTTCs lead to decreased saltation length, we expect that a tight regulation of LTCC activity is required to optimally handle intracellular calcium, engage calcium-dependent cytoskeletal machinery and achieve efficient interneuron migration steps.

Excess phosphorylation of myosin light chain influences saltation length, but not saltation frequency, of TS cortical interneurons

We next asked whether downstream changes in cell-rear actomyosin signaling mediates the saltation length phenotype in TS. Calcium-bound calmodulin activates myosin light-chain kinase (MLCK), which in turn phosphorylates myosin light chain (MLC) and induces MLC interaction with F-actin and contraction at the soma rear (Figures 3A and 3B). We reasoned that increased $[Ca^{2+}]_i$ in TS interneurons may lead to excess phosphorylation of MLC, aberrant actomyosin function, and, consequently, reduced saltation length. To test this, we first quantified pMLC2s19 levels, which have been previously shown to correlate with myosin ATPase activity and contractility (Tan et al., 1992). Western blotting of protein lysates extracted from whole hSSs (2–3 hSSs pooled per sample) revealed increased pMLC2s19 levels in TS hSS (Figures 3C, 3D, and S3A, $p < 0.05$). Immunocytochemistry for pMLC2s19 in MAP2$^+$ neuronal soma of plated hSSs also showed an increase in pMLCs19 levels in TS neurons (Figures 3E–3G, Base Ctrl versus Base TS: $p < 0.0001$). Moreover, a 15 min application of FPL 64176 (5 μM) on plated hSS neurons induced an increase in pMLC2s19 levels in Ctrl interneurons, demonstrating a link between MLC phosphorylation and LTCC activation (Figure 3G, Ctrl Base versus FPL: $p < 0.01$). Of note, we found no detectable increase of pMLC2s19 levels in TS interneurons treated with FPL 64176, which is likely due to saturation of pMLC2s19 levels in TS. Finally, we asked if inhibiting MLC phosphorylation would be sufficient to restore saltation length and/or frequency in TS. We found that application of ML-7 (5 μM), a selective MLCK inhibitor, increased the saltation length but had no effect on the saltation frequency of TS interneurons (Figures 3H and 3I, Ctrl saltation length: $p < 0.0001$; TS saltation length: $p < 0.0001$), further emphasizing that two components of the TS migration phenotype are likely mediated by different molecular pathways downstream of the TS $Ca_v1.2$ channel.

Transcriptional profiling suggests changes in GABA receptor signaling and membrane potential in TS hSS

Given that the TS saltation frequency phenotype remained unchanged upon acute modulation of LTCC function, $[Ca^{2+}]_i$ levels, and actomyosin function, we asked whether there are other independent pathways that could instead explain the increased saltation frequency in TS interneurons. To further investigate this, we performed RNA sequencing on hCSs and hSSs derived from 3 individuals with TS and 6 Ctrl individuals across early (days 40–75) and late (days 90–129) differentiation stages (time points), as well as hSS samples that were chemically depolarized with 67 mM KCl for 6 h (Figure 4A; Table S1 includes detailed sample information). We first performed a series of quality-control (QC) analyses to validate sample-matching (Figure S4A), confirm the presence of the TS mutation (Figure S4B), and profile ancestral diversity (Figure S4C). We also assessed variability across lines (Figures S4D–S4F), as well as differentiation efficiency (Figure S4G). Finally, we analyzed the proportion of variation explained by the different covariates using variance partitioning (Figure S4H). We found that differentiation (experimental batches) and differentiation length explained a median of 11% and 6% of variability, respectively, while differentiation

Please cite this article in press as: Birey et al., Dissecting the molecular basis of human interneuron migration in forebrain assembloids from Timothy syndrome, Cell Stem Cell (2021), https://doi.org/10.1016/j.stem.2021.11.011

CellPress

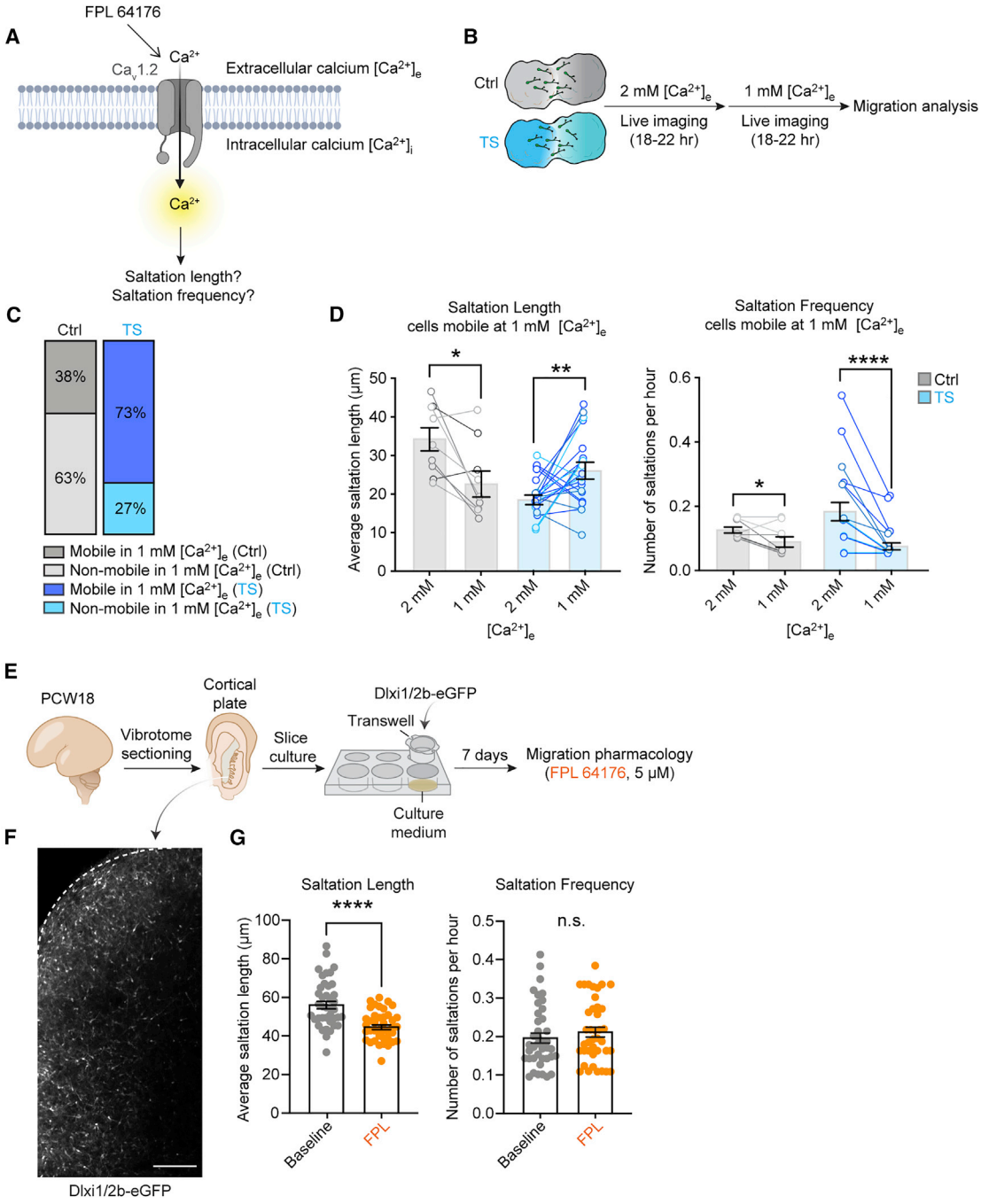

Figure 2. Acute modulation of intracellular calcium levels influences saltation length, but not saltation frequency, in TS interneurons

(A) Schematic illustrating the presumptive direct effect of intracellular calcium influx on saltation length and/or frequency.

(B) Schematic illustrating the migration imaging experiment in modified extracellular calcium concentrations ($[Ca^{2+}]_e$).

(C) Proportion of Ctrl and TS interneurons that are either mobile (>1 saltation) or non-mobile in 1 mM $[Ca^{2+}]_e$ (chi-square test, $\chi^2 = 7.0$, $^{**}p < 0.01$).

(D) Quantification of saltation length and frequency at 1 mM $[Ca^{2+}]_e$ (Ctrl, n = 9 cells from 4 hiPSC lines, 1–3 assembloid per line; TS, n = 22 cells from 3 hiPSC lines, 1–3 assembloid per line. Paired t test, $^{*}p < 0.05$, $^{**}p < 0.01$, $^{****}p < 0.0001$).

(E) Schematic illustrating the *ex vivo* primary fetal cortical slice culture protocol to perform interneuron migration imaging coupled with FPL 64176 administration.

(F) Representative live migration imaging snapshot showing migrating Dlxi1/2b-eGFP$^+$ interneurons in a primary human cortical slice.

(G) Quantification of saltation length and frequency following FPL 64176 administration (n = 40 cells from 4 fields across 1 cortical section. Two-tailed t test, $^{****}p < 0.0001$). Scale bar: 100 μm in (F). n.s., not significant. For (D), different shades of gray represent individual Ctrl hiPSC lines. Different shades of cyan represent individual TS hiPSC lines.

Please cite this article in press as: Birey et al., Dissecting the molecular basis of human interneuron migration in forebrain assembloids from Timothy syndrome, Cell Stem Cell (2021), https://doi.org/10.1016/j.stem.2021.11.011

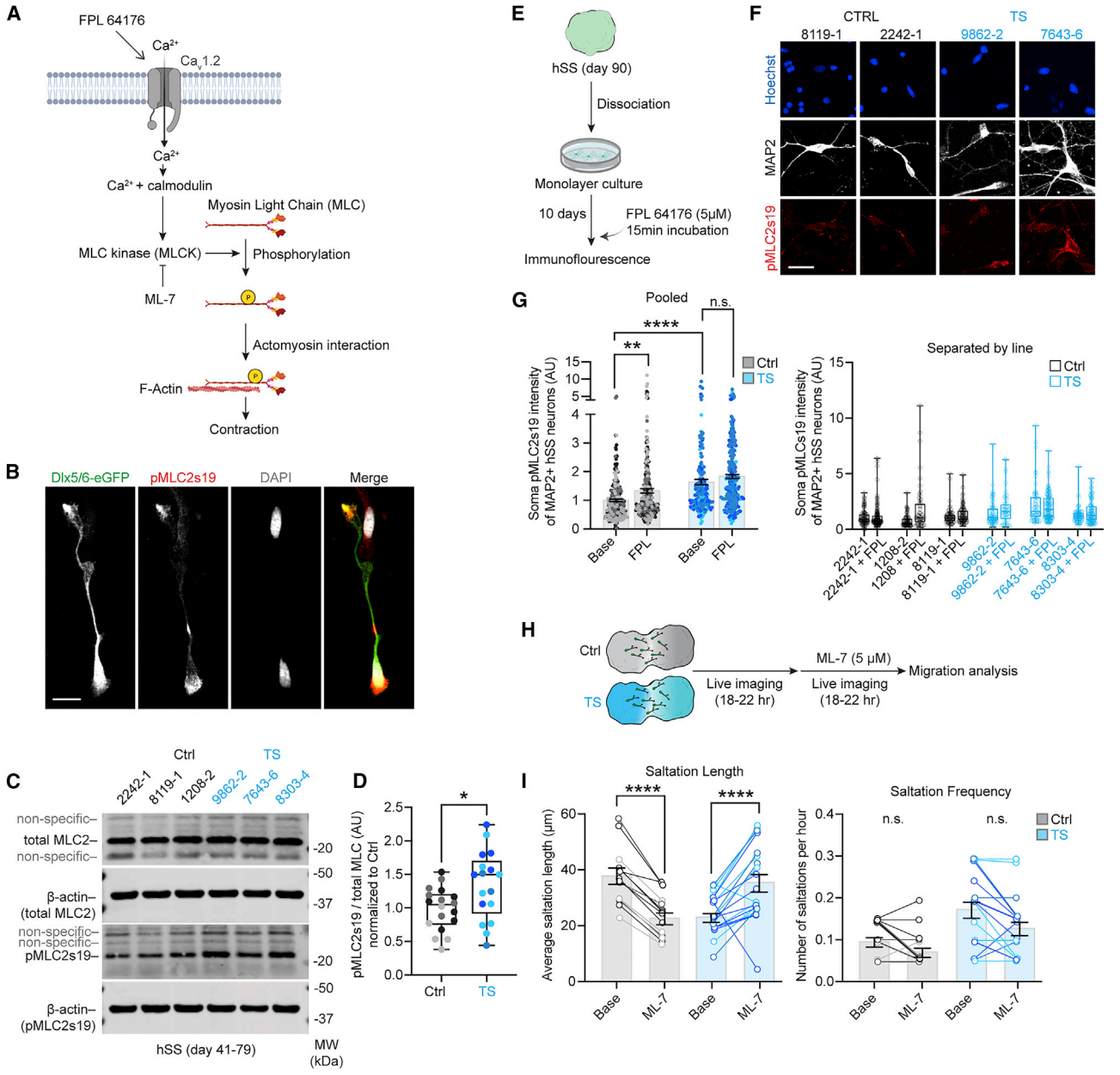

Figure 3. MLC hyper-phosphorylation at the cell rear is related to the saltation length, but not saltation frequency, in TS interneurons

(A) Schematic illustrating the effect of calcium on the actomyosin contractility pathway.

(B) Representative immunocytochemistry images of pMLC2s19 localized to Dlx5/6-eGFP^{+} interneurons on plated Ctrl hSS (day 101).

(C) Representative images of western blot scans showing total MLC2, pMLC2s19, and β-actin protein levels from Ctrl and TS hSS.

(D) Western blot quantification of the ratio of pMLC2s19 and total MLC2 protein levels in hSS (days 41–79). Values normalized to Ctrl levels per run (Ctrl, n = 18 samples from 3 hiPSC lines, 2–3 hSSs per sample; TS, n = 18 samples from 3 hiPSC, 2–3 hSSs pooled per sample). Two-tailed t test, *p < 0.05).

(E) Schematic illustrating the FPL 64176 stimulation experiment.

(F) Representative immunocytochemistry images of pMLC2s19 and MAP2 from plated hSS neurons (day 90).

(G) Quantification of pMLC2s19 levels in MAP2^{+} somas at baseline or after FPL 64176 stimulation (left: pooled, right: separated by line. Ctrl, n = 237 cells from 3 hiPSC lines; Ctrl + FPL, n = 269 cells from 3 hiPSC lines; TS, n = 198 cells from 3 hiPSC lines; TS + FPL, n = 275 cells from 3 hiPSC lines, 2–3 hSSs pooled per line per condition. Two-way ANOVA; $F_{1, 975} = 12.18$, $F_{1, 782} = 128$, **p < 0.01, ****p < 0.0001).

(H) Schematic illustrating the interneuron migration imaging coupled with ML-7 pharmacology.

(I) Quantification of saltation length and frequency following ML-7 administration (Ctrl, n = 14 cells from 4 hiPSC lines, 1–4 assembloid per line; TS, n = 21 cells from 3 hiPSC lines, 1–3 assembloid per line. Paired t test, ****p < 0.0001). Bar charts: mean ± SEM. Boxplots: center, median; lower hinge, 25% quantile; upper hinge, 75% quantile; whiskers; minimum and maximum values. Scale bars: 10 μm in (B) and 20 μm in (F) . n.s., not significant. For (D), (G), and (I), different shades of gray represent individual Ctrl hiPSC lines. Different shades of cyan represent individual TS hiPSC lines.

Please cite this article in press as: Birey et al., Dissecting the molecular basis of human interneuron migration in forebrain assembloids from Timothy syndrome, Cell Stem Cell (2021), https://doi.org/10.1016/j.stem.2021.11.011

CellPress

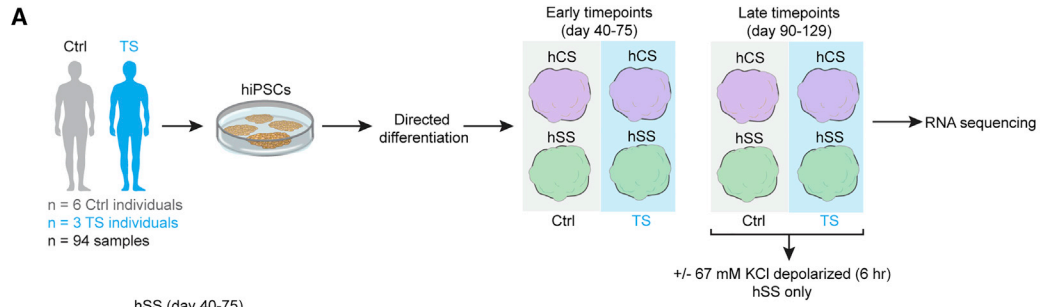

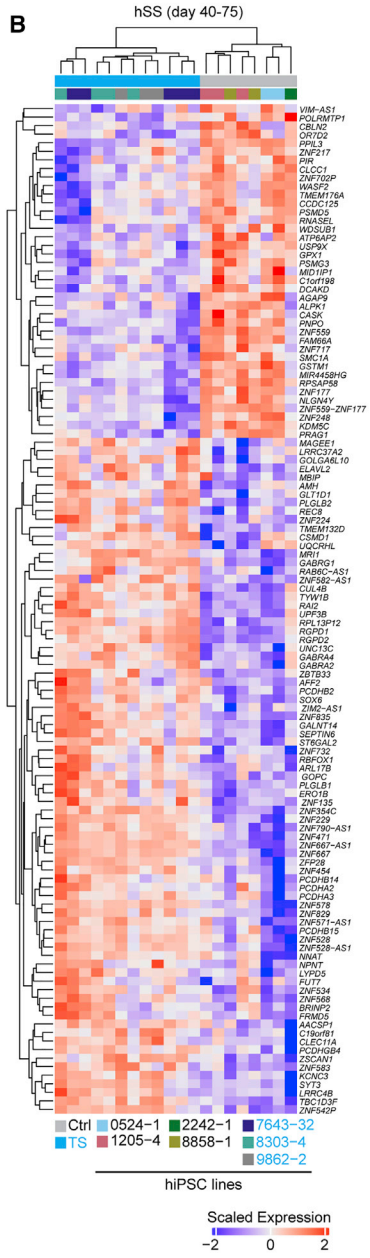

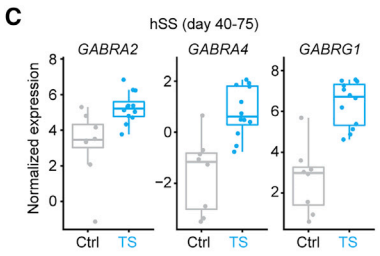

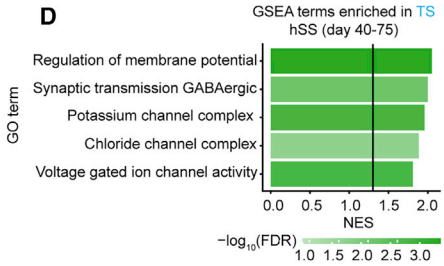

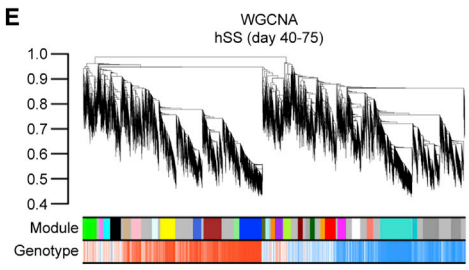

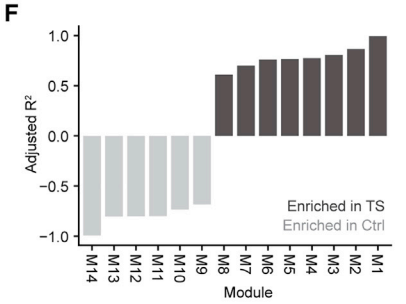

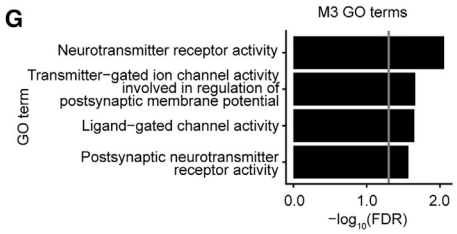

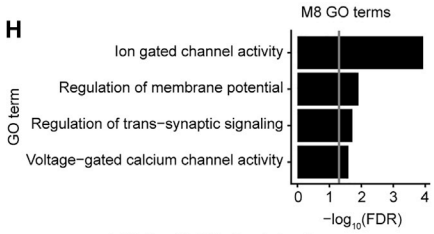

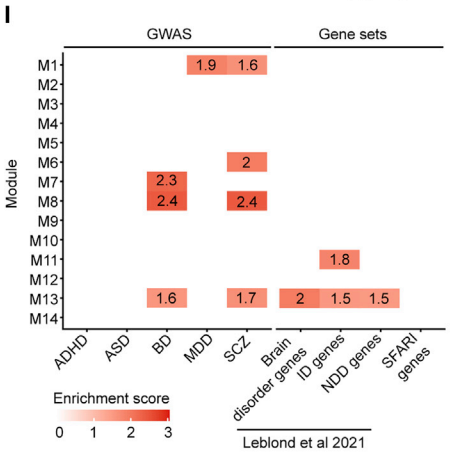

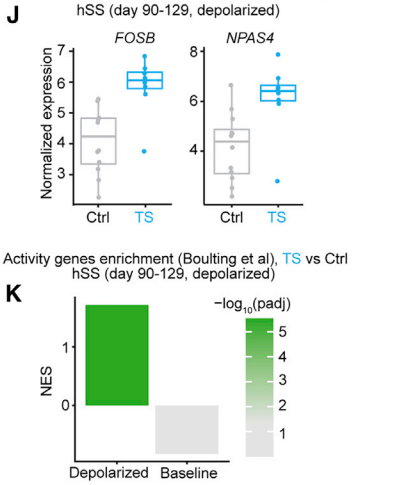

(legend on next page)

Please cite this article in press as: Birey et al., Dissecting the molecular basis of human interneuron migration in forebrain assembloids from Timothy syndrome, Cell Stem Cell (2021), https://doi.org/10.1016/j.stem.2021.11.011

fate (hCS versus hSS), activation state (depolarization), and genotype (Ctrl versus TS) explained less than a median of 5% of variability.

We first inspected differential expression in hSS samples at early time points corresponding to the stages of differentiation during which we have performed the migration experiments. Among differentially expressed genes, we found upregulation of 3 genes encoding GABA receptor subunits (*GABRA4*: logFC = 3.1, FDR = 0.0002; *GABRA2*: logFC = 2.2, FDR = 0.007; *GABRG1*: logFC = 4.0, FDR = 0.0006; Figures 4B and 4C; Table S2). Gene set enrichment analysis (GSEA) further indicated a robust enrichment of genes associated with GABA transmission ("synaptic transmission GABAergic" and "chloride channel complex") as well as resting membrane potential (RMP) ("regulation of membrane potential" and "voltage-gated ion channel activity") in hSS (Figure 4D; Table S3), but not in hCS where we found, primarily, upregulation of glutamate receptor signaling changes (Figure S4I; Table S3). Previous work has shown that gene co-expression relationships of gene expression can be leveraged to better understand disease biology (Zhang and Horvath, 2005; Voineagu et al., 2011; Parikshak et al., 2015). In light of this, we performed weighted gene co-expression network analysis (WGCNA) to identify modules of highly correlated genes in the hSS dataset. This analysis identified 14 modules that were significantly associated with TS (FDR < 0.05; Figures 4E and 4F; Table S4), 8 of which were upregulated in TS. Congruent with GSEA results, Gene Ontology terms for the upregulated modules included "neurotransmitter receptor activity" and "transmitter-gated ion channel activity involved in the regulation of postsynaptic membrane potential" (Module M3; Figure 4G) as well as "ion gated channel activity" and "regulation of membrane potential" (Module M8; Figure 4H). Modules M1, M6, M7, and M8 (adjusted R^2_{M1} = 0.99, adjusted R^2_{M6} = 0.76, adjusted R^2_{M7} = 0.7, and adjusted R^2_{M8} = 0.61), which were upregulated in TS hSS as well as M13 (adjusted R^2_{M8} = −0.8), which was down regulated in TS hSS, were enriched for SNP heritability on the basis of genome-wide association studies (GWAS) (BD, bipolar disorder; MDD, major depressive disorder; SCZ, schizophrenia; $M1_{MDD}$Enrichment = 1.9, FDR = 1.0×10^{-3}; $M1_{SCZ}$Enrichment = 1.6, FDR = 5.0×10^{-3}; $M6_{SCZ}$ Enrichment = 2.0, FDR = 9.2×10^{-3}; $M7_{BD}$Enrichment = 2.3, FDR = 2.8×10^{-2}; $M8_{BD}$Enrichment = 2.4, FDR = 2.3×10^{-2}; $M8_{SCZ}$Enrichment = 2.4, FDR = 1.1×10^{-2}; $M13_{BD}$Enrichment = 1.6, FDR = 1.1×10^{-2}; $M13_{SCZ}$Enrichment = 1.7, FDR = 1.1×10^{-2}). Modules M11 and M13 were also enriched for genes associated with NDD and intellectual disability (ID) genes (Leblond et al., 2021) (brain disorder genes: OR_{M13} = 2, FDR = 1.4×10^{-2}; NDD genes: OR_{M13} = 1.5, FDR = 3.7×10^{-4}; ID genes: OR_{M13} = 1.5, FDR = 3.7×10^{-4}, OR_{M11} = 1.8, FDR = 3.5×10^{-2}) (Figure 4I). Taken together, these results indicate that the TS $Ca_v1.2$ channel could alter specific transcriptional programs in hSS.

Activity-dependent gene expression programs are tightly regulated by $Ca_v1.2$ and associated calcium signaling pathways (Dolmetsch, 2003; Yap and Greenberg, 2018) and have been previously shown to be altered in TS (Paşca et al., 2011; Servili et al., 2020). For example, cAMP response element-binding protein (CREB) is known to modulate gene expression via calcium influx-mediated phosphorylation (Wheeler et al., 2012). To probe potential changes in calcium signaling-mediated gene expression pathways in TS hSS, we first quantified phospho-CREB-ser133 (pCREBs133) levels in Dlxi1/2b-eGFP$^+$ interneurons and found that they were significantly higher in TS interneurons ($p < 0.0001$; Figures S4J and S4K). Next, we used chemical depolarization by exposing intact hSSs (2–3 hSSs per sample) to high-potassium Tyrode's solution containing 67 mM KCl for either 1 h or 6 h. Depolarization induces intracellular calcium influx through LTCC and non-LTCC pathways, such as N-Methyl-D-aspartate (NMDA) receptors and calcium-permeable α-amino-3-hydroxy-5-methyl-4-isoxazolepropionic acid (AMPA) receptors (Yap and Greenberg, 2018). To resolve the contribution of LTCCs, we also separately applied Nim during depolarization (Figure S4L). These experiments revealed significantly enhanced induction of activity-regulated genes such as *FOS* and *NPAS4* in TS relative to Ctrl at the 6 h time point, which was inhibited by Nim (Figure S4M). We did not detect differences between Ctrl and TS at the 1 h time point. We next tested for enrichment for the activity-dependent regulome of human GABAergic neurons described by Boulting et al. (2021) using GSEA on a subset of hSS samples depolarized with 67 mM for 6 h. We found significant enrichment for the activity-dependent programs in the upregulated genes in TS only after depolarization (Figures 4J and 4K), in line with qPCR results (Figures S4L and S4M). Overall, these results suggested upregulation of transcriptional programs related to GABA neurotransmission, ion channel activity, and resting membrane potential in TS interneurons, potentially through altered recruitment of LTCC-related, activity-dependent transcriptional programs.

Modulation of GABA-A receptor function decreases saltation frequency in TS cortical interneurons

To functionally validate changes in gene expression in hSS, we performed calcium imaging in interneurons in intact hSSs

Figure 4. Altered gene expression in TS hSS

(A) Schematic illustrating the experimental design for the RNA sequencing experiments.
(B) Heatmap of expression of the top differentially expressed genes (DEGs) based on hierarchical clustering in hSS samples from early time points.
(C) Boxplots showing differential expressed GABA receptor subunits in hSS (FDR < 0.05).
(D) Select genes from GSEA in hSS samples from early time points showing enriched terms in TS. Line indicates FDR = 0.05.
(E) Dendrogram illustrating the significant WGCNA modules.
(F) Coefficient of determination (adjusted R^2) of WGCNA modules that are significantly associated with TS (FDR < 0.05).
(G) Module M3 GO terms enriched in TS. Line indicates FDR = 0.05.
(H) Module M8 GO terms enriched in TS. Line indicates FDR = 0.05.
(I) Enrichment for the GWAS signal from attention deficit hyperactivity disorder (ADHD), ASD, BD, MDD, and SCZ as well as other disease-associated gene sets. Numbers and colors represent the enrichment score (FDR < 0.05).
(J) Boxplots showing differential expressed activity-dependent genes *FOSB* and *NPAS4* in depolarized hSSs.
(K) Activity gene enrichment of depolarized hSS samples compared with Boulting et al. (2021) dataset. Boxplots: center, median; lower hinge, 25% quantile; upper hinge, 75% quantile; whiskers extend to ±1.5× interquartile range.

Please cite this article in press as: Birey et al., Dissecting the molecular basis of human interneuron migration in forebrain assembloids from Timothy syndrome, Cell Stem Cell (2021), https://doi.org/10.1016/j.stem.2021.11.011

CellPress

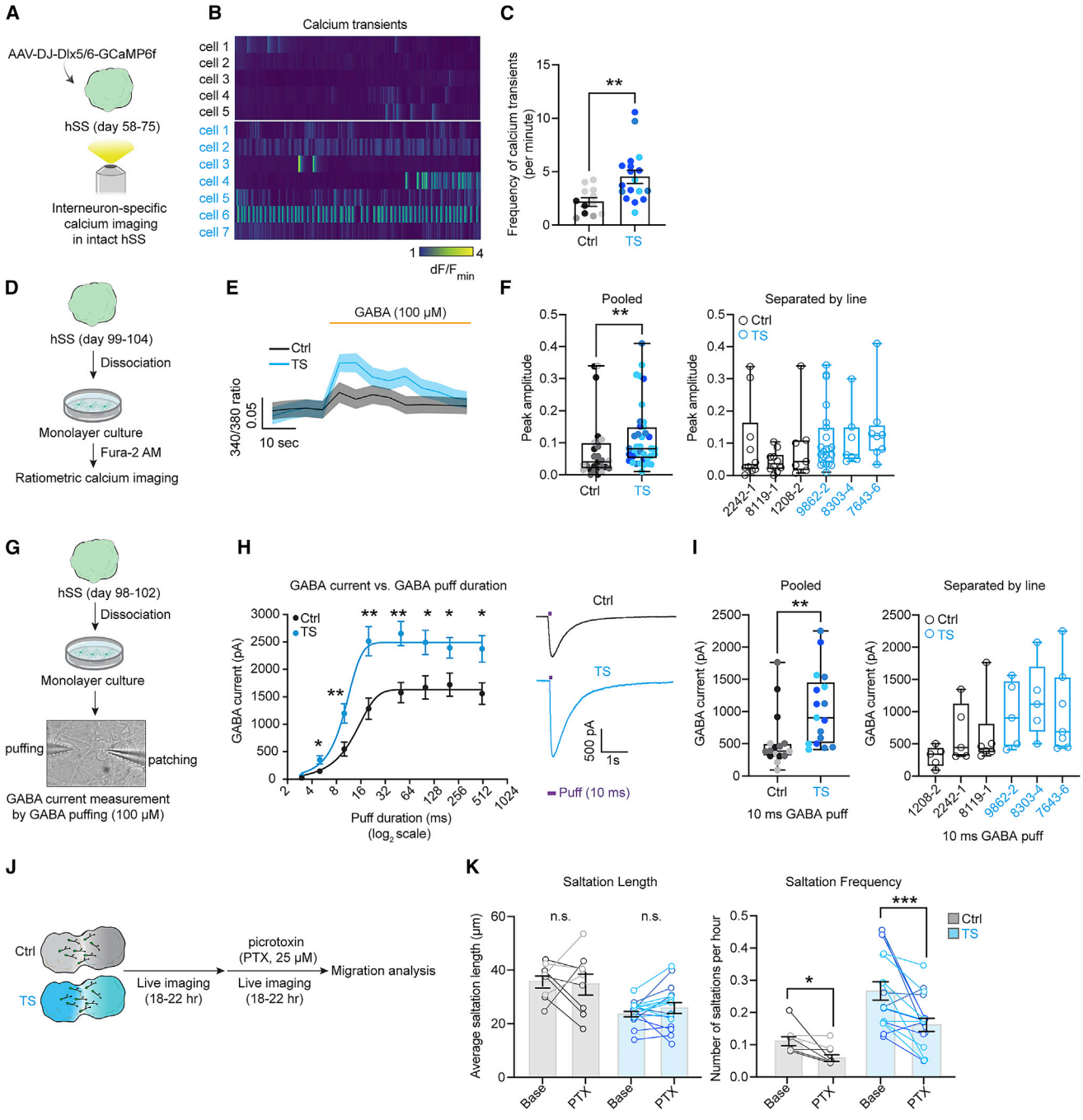

Figure 5. Blocking GABA-A receptors restores saltation frequency but not saltation length in TS interneurons

(A) Schematic illustrating the calcium imaging experiment in intact hSS using a interneuron-specific calcium indicator (Dlx5/6-GCaMP6f).

(B) Heatmap showing representative calcium transients.

(C) Quantification of calcium transient frequency (Ctrl, n = 12 cells from 4 hiPSC lines; TS, n = 19 cells from 3 hiPSC lines, 2–3 hSSs per line. Mann-Whitney test, $^{**}p < 0.01$).

(D) Schematic illustrating the Fura-2 calcium imaging and GABA pharmacology on plated hSS cells.

(E) Changes in Fura-2 ratio in response to 100 μM GABA in plated hSS cells (days 99–104).

(F) Quantification of peak amplitudes corresponding to changes in Fura-2 ratio in response to 100 μM GABA (left: pooled, right: separated by line. Ctrl, n = 27 responding cells from 3 hiPSCs; TS, n = 35 responding cells. 2–3 hSSs pooled per line. Mann-Whitney test, $^{**}p < 0.01$).

(G) Schematic illustrating the GABA puffing experiments on plated hSS cells (days 98–102).

(H) Left: GABA current versus puff duration plots (Ctrl, n = 16 cells from 3 hiPSC lines; TS, n = 17 cells from 3 hiPSC lines. 2–3 hSSs pooled per line. Two-tailed t test per puff duration, $^{*}p < 0.05$, $^{**}p < 0.01$. Two-way ANOVA for puff times [20 ms puff values excluded due to unequal number of cells in Ctrl versus TS groups],

(legend continued on next page)

Please cite this article in press as: Birey et al., Dissecting the molecular basis of human interneuron migration in forebrain assembloids from Timothy syndrome, Cell Stem Cell (2021), https://doi.org/10.1016/j.stem.2021.11.011

labeled with a genetically encoded calcium indicator (GCaMP) (Figure 5A) and found an increased rate of spontaneous calcium transients in TS (Figures 5B and 5C, $p < 0.01$). We then performed whole-cell patch clamping to investigate the intrinsic electrophysiological properties of Dlxi1/2b-eGFP$^+$ migrating interneurons in intact forebrain assembloids. We placed forebrain assembloids on cell culture inserts (transwells) for 7–14 days to achieve a flattened geometry that is more amenable to patch-clamping migrating interneurons in intact 3D assembloids (Figures S5A and S5B). Most interneurons fired single action potentials although interneurons with repetitive firing were also observed in both Ctrl and TS assembloids (Figures S5C and S5D). Importantly, in line with the transcriptional changes suggestive of altered membrane potential and ion channel activity in hSS (Figures 4D, 4G, and 4H), we observed that the RMP in TS was relatively depolarized while the capacitance and input resistance remained unchanged (Figure S5E; RMP: $p < 0.0001$). Interestingly, TS hCS neurons did not show the same difference in RMP (Figures S5F and S5G), possibly pointing to neuron subtype-specific changes associated with the TS mutation.

Considering that ambient GABA influences interneuron migration (Manent et al., 2005; Cuzon et al., 2006; Heck et al., 2007; Bortone and Polleux, 2009) and that our results suggested gene expression changes in GABA receptors in TS hSS, we next asked whether changes in GABA neurotransmission could underlie the saltation frequency phenotype in TS. GABA has been shown to be depolarizing in developing interneurons (Bortone and Polleux, 2009). Indeed, application of 1 mM GABA to an intact hSS labeled with an interneuron-specific GCaMP (Dlxi1/2b-mScarlet-P2A-GCaMP6s) revealed that GABA is depolarizing in hSS interneurons at this stage of development (Video S3). We verified the effect of GABA application on calcium activity using ratiometric imaging (Fura-2) in plated hSS cells (Figure 5D; proportion of TUJ1$^+$ cells out of DAPI$^+$cells: Ctrl = 80.74%; TS = 79.06%; proportion of GABA$^+$ cells out of TUJ1$^+$ cells: Ctrl = 94.38%; TS = 93.62%) (Figures S5H and S5I). We found that 100 μM GABA could induce a rise in calcium influx in a subset of cells (Figure 5E). Importantly, the amplitude of the GABA-induced calcium rise was higher in TS cells (Figure 5F, $p < 0.01$), suggesting enhanced GABA-induced calcium influx in TS. To further verify the enhanced effect of GABA on TS interneurons, we used whole-cell patch clamping and puff-applied 100 μM GABA (Figure 5G). We found larger GABA-induced currents in TS across various puff durations (Figures 5H and 5I, 5 ms: $p < 0.05$, 10 ms: $p < 0.01$, 20 ms: $p < 0.01$, 50 ms: $p < 0.01$, 100 ms: $p < 0.05$, 200 ms: $p < 0.05$, 500 ms: $p < 0.05$). Overall, these results suggested enhanced GABA sensitivity in TS.

Finally, we wondered if modulating GABA receptor activity could restore the saltation frequency phenotype of TS interneurons. We first performed migration imaging in the presence of GABA-A receptor blocker picrotoxin (PTX) (25 μM; Figure 5J) and discovered that this restored the saltation frequency but had no effect on saltation length of TS interneurons. Of note, saltation frequency in Ctrl interneurons was also reduced (Figure 5K, Ctrl saltation frequency: $p < 0.05$; TS saltation frequency: $p < 0.001$), which is expected given the role of GABA receptors in interneuron migration. To further validate GABA receptor-mediated modulation of saltation frequency, we also used a second GABA-A blocker, bicuculine (50 μM; Figure S5J) and found a similar effect on saltation frequency but no effect on saltation length (Figure S5K; Ctrl saltation frequency: $p < 0.01$; TS saltation frequency: $p < 0.05$). In conclusion, we find that two distinct pathways underlie the inefficient migration phenotype in TS interneurons: (1) calcium influx through LTCC acutely regulates actomyosin function and saltation length, and (2) GABA receptor signaling mediates saltation frequency and overall motility.

Abnormal activity in TS cortical networks in forebrain assembloids

Given the prominent roles $Ca_V1.2$ plays in neural development (Bates, 2015; Panagiotakos et al., 2019), we next asked whether the TS mutation is associated with changes in transcriptional maturation trajectories. We applied two separate RNA sequencing-based comparative analyses to assess interneuron maturation from early to late stages of differentiation (d40–d129). First, we used the interneuron maturation markers described in Mi et al. (2018), which revealed no significant differences in the expression of interneuron maturation or progenitor markers between genotypes (Figure S6A). Next, we applied the interneuron maturation score described in Mayer et al. (2018), which is based on sequential gene expression in ganglionic eminences in mice. We calculated the eigengene for each gene group in our data and found no major differences in maturation trajectories across genotypes (Figure S6B). We also detected no differences in *SLC12A5/SLC12A2* ratio across stages of differentiation suggesting that chloride reversal potential may not be affected in TS (Figure S6C). Next, to assess potential differences in the composition of interneuron subtypes in Ctrl versus TS, we quantified the proportion of calbindin$^+$, calretinin$^+$, and somatostatin$^+$ cells in plated hSS cells by immunocytochemistry and found no differences (Figures S6D and S6E). Overall, these results indicate that there are likely no major differences in the developmental trajectories of cortical interneurons in TS.

Lastly, to assess the network-level dynamics and the impact of infiltrating interneurons on these dynamics in TS forebrain assembloids, we performed calcium imaging in hCS neurons

$F_{15, 105} = 12.74$, ****$p < 0.0001$. Curve was fitted using the Boltzmann sigmoid equation). Right: representative GABA current traces in response to 10 ms GABA puff.

(I) Quantification of GABA current amplitudes in response to 10 ms GABA puff (left: pooled, right: separated by line. Ctrl, n = 16 cells from 3 hiPSC lines; TS, n = 17 cells from 3 hiPSC lines. 2–3 hSSs pooled per line. Mann-Whitney test, **$p < 0.01$).

(J) Schematic illustrating the migration imaging and PTX pharmacology.

(K) Quantification of saltation length and frequency following PTX administration (Ctrl, n = 9 cells from 3 hiPSC lines, 1–2 assembloid per line; TS, n = 17 cells from 3 hiPSC lines, 1–2 assembloid per line. Paired t test, *$p < 0.05$, ***$p < 0.001$). Bar charts: mean ± SEM. Boxplots: center, median; lower hinge, 25% quantile; upper hinge, 75% quantile; whiskers; minimum and maximum values. n.s., not significant. For (C), (F), (I), and (K) different shades of gray represent individual Ctrl hiPSC lines. Different shades of cyan represent individual TS hiPSC lines.

Please cite this article in press as: Birey et al., Dissecting the molecular basis of human interneuron migration in forebrain assembloids from Timothy syndrome, Cell Stem Cell (2021), https://doi.org/10.1016/j.stem.2021.11.011

CellPress

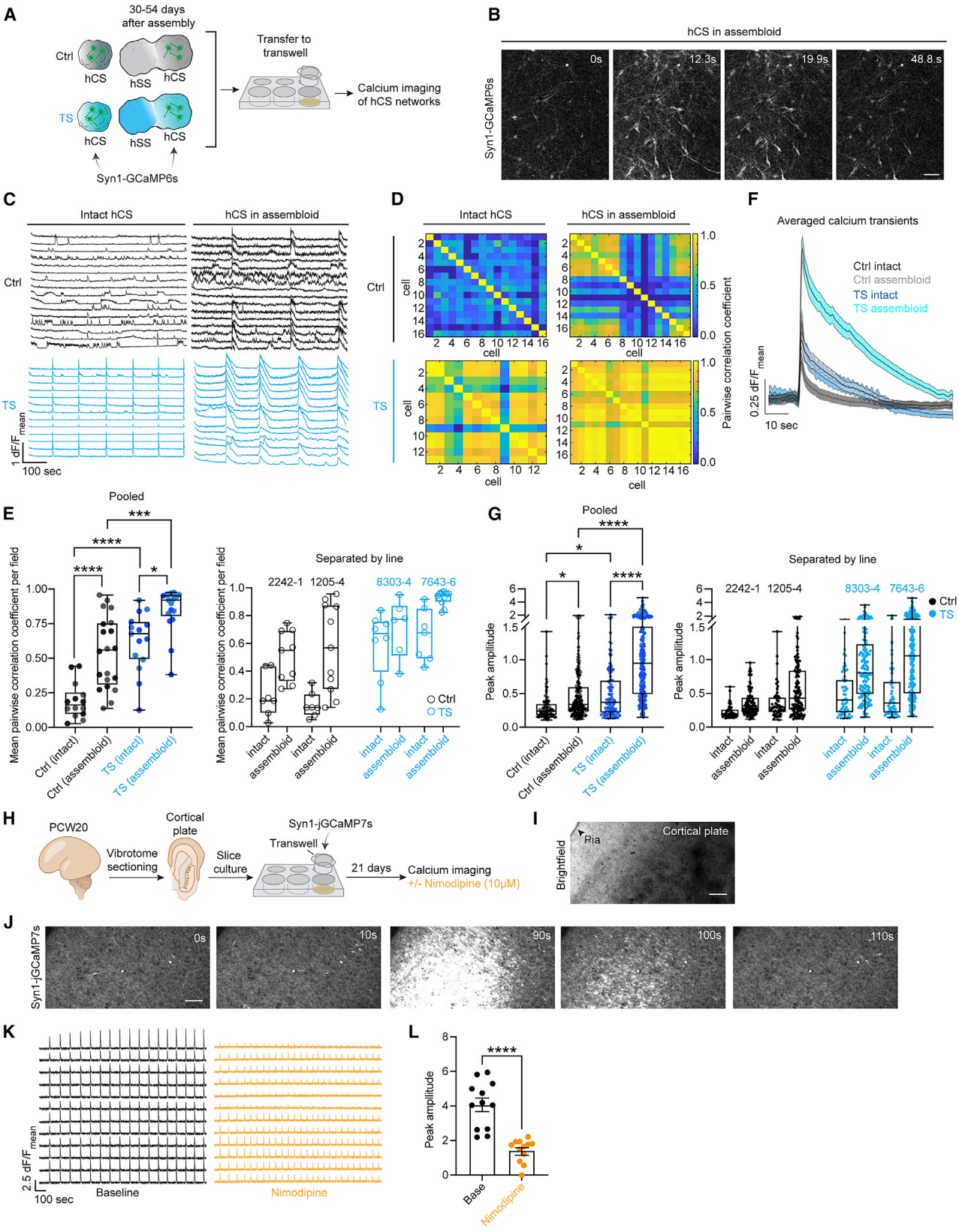

(legend on next page)

Please cite this article in press as: Birey et al., Dissecting the molecular basis of human interneuron migration in forebrain assembloids from Timothy syndrome, Cell Stem Cell (2021), https://doi.org/10.1016/j.stem.2021.11.011

labeled with Syn1-GCaMP6s either in intact hCSs or in hCSs following assembly with hSSs (Figures 6A and 6B). By measuring mean pairwise Pearson's correlation coefficients of activity per imaging field, we observed an increase in the correlated activity in assembled hCSs compared with intact hCSs in Ctrl, confirming the excitatory role of GABA at this stage of development (Figure 5E). Interestingly, we found that activity in intact TS hCSs was characterized by hypersynchronous events, and this was further enhanced following assembly with hSS (Figures 6C–6E). We also asked whether the amplitudes of the calcium transients were altered in TS hCS neurons following assembly with hSS. We found that assembly with hSS increased the amplitude of calcium events in both Ctrl and TS hCSs (Figures 6F and 6G), but this effect was enhanced in TS compared with Ctrl ($p < 0.0001$). Finally, we asked how pharmacological modulation of LTCC impacts network activity in *ex vivo* primary human cortex (Figure 6H). Imaging of hSyn1-jGCaMP7s-labeled cortical neurons revealed synchronous activity as well as uncorrelated transients in *ex vivo* primary human cortical networks at PCW20, similar to what we observed in forebrain assembloids (Figures 6I and 6J). Application of the LTCC blocker Nim (10 μM) robustly reduced the amplitude of correlated calcium transients (Figures 6K and 6L). In summary, in line with the role of LTCCs in driving synchronous activity in *ex vivo* human cerebral cortex (Figure 6K), we find that TS hCS networks display highly synchronous activity that is further enhanced after assembly with hSS.

Overall, we propose that impaired arrival and altered intrinsic properties of interneurons in TS could impact emerging cortical circuits and lead to aberrant network dynamics. We discover that activity in hCS networks in TS is hypersynchronous, which is further exacerbated following migration of neurons from hSSs. The migration defect in TS interneurons may also result in changes in the number of functionally integrated interneurons in the dorsal forebrain that, in combination with changes in their intrinsic electrophysiological properties and response to GABA, may adversely impact the inhibitory tone in cortical networks and potentially lead to seizures. Although it is difficult to ascertain circuit-level, seizure-inducing phenotypes from *in vitro* experiments, our results point to altered neuronal intrinsic properties and cell-cell interactions in TS that may promote hyperexcitability in emerging cortical networks.

DISCUSSION

Various genetic and environmental factors have been proposed to perturb GABAergic cortical interneuron development and lead to neuropsychiatric disease, including ASD, SCZ, and epilepsy (Marín, 2012). The unique features of interneurons in primates (Silbereis et al., 2016; Krienen et al., 2020; Hodge et al., 2019) and the lack of patient-derived tissue preparations have limited our mechanistic understanding of the role of cortical interneurons in disease. We have previously developed forebrain assembloids (Birey et al., 2017)—an hiPSC-derived 3D culture platform where region-specific spheroids can be assembled to model the migration and functional integration of human cortical interneurons. We have also sought to study interneuron migration in forebrain assembloids derived from patients with TS—a rare and highly penetrant form of monogenic ASD and epilepsy. TS is caused by a gain-of-function mutation (G406R) in the alternatively spliced exon 8a of *CACNA1C*, which encodes for the α subunit of the LTCC $Ca_v1.2$. Voltage-gated calcium channels have previously been implicated in regulating interneuron migration (Bortone and Polleux, 2009; Kamijo et al., 2018). Using TS forebrain assembloids, we discovered that the TS $Ca_v1.2$ channel leads to a compound migration phenotype associated with the saltatory mode of migration in cortical interneurons, namely decreased saltation length and increased saltation frequency (Birey et al., 2017). We now report that the decreased saltation length in TS is driven by an acute increase in calcium influx through LTCCs, followed by aberrant actomyosin function at the soma rear and the uncoupling of soma rear-front coordination during nucleokinesis; in contrast, the increased saltation frequency phenotype in TS is mediated by enhanced GABA receptor signaling (Figure 7).

Signaling localized to specific cellular compartments (e.g., growth cone and soma) may differentially affect migratory behavior. For example, coordinated interaction between actin/myosin and microtubules is essential for a variety of dynamic cellular processes, such as motility, division, and adhesion

Figure 6. Abnormal hCS activity in TS forebrain assembloids

(A) Schematic illustrating the calcium imaging of hCS networks in intact hCS and in hCS assembled with hSS, each virally labeled with Syn1-GCaMP6s.
(B) Representative snapshots of GCaMP imaging in hCS assembled with hSS showing synchronous network activity.
(C) Representative traces of activity from intact hCS and hCS assembled with hSS derived from Ctrl and TS hiPSC lines.
(D) Pairwise correlation coefficient plots showing correlated activity in representative fields.
(E) Quantification of mean pairwise correlation coefficient per field (left: pooled, right: separated by line. Intact: Ctrl, n = 14 fields from 2 hiPSC lines, 3 hCSs per line. Intact: TS, Ctrl, n = 15 fields from 2 hiPSC lines, 3–4 hCSs per line. Assembloid: Ctrl, n = 20 fields from 2 hiPSC lines, 3–5 assembloids per line. Assembloid: TS, n = 17 fields from 2 hiPSC lines, 3–5 assembloids per line. Two-way ANOVA; $F_{1, 62} = 32.38$ (for intact versus assembloid), $F_{1, 62} = 53.73$ (Ctrl versus TS), *$p < 0.05$, ***$p < 0.001$, ****$p < 0.0001$.
(F) Averaged calcium traces. Line represents the mean, shaded margins show the 95% confidence interval.
(G) Quantification of averaged peak amplitude per cell (left: pooled, right: separated by line. Intact: Ctrl, n = 97 cells from 2 hiPSC lines, 3 hCSs per line. Intact: TS, Ctrl, n = 111 cells from 2 hiPSC lines, 3–4 hCSs per line. Assembloid: Ctrl, n = 239 cells from 2 hiPSC lines, 3–5 assembloids per line. Assembloid: TS, n = 339 cells from 2 hiPSC lines, 3–5 assembloids per line. Two-way ANOVA; $F_{1, 782} = 116.7$, $F_{1, 782} = 128$, *$p < 0.05$, ***$p < 0.001$, ****$p < 0.0001$).
(H) Schematic illustrating imaging and pharmacological manipulation in *ex vivo* primary fetal cortical slices.
(I) Brightfield image of the cortical plate in primary human cortical slices.
(J) Representative snapshots of GCaMP imaging in the primary human cortical slices showing synchronous network activity.
(K) Representative traces of calcium activity in primary human cortical slices showing synchronous network activity before and after Nim administration.
(L) Quantification of averaged peak amplitude per cell before and after Nim administration (Ctrl, n = 12 cells from 1 field and 1 section). Two-tailed t test, ****$p < 0.0001$. Boxplots: center, median; lower hinge, 25% quantile; upper hinge, 75% quantile; whiskers; minimum and maximum values. Scale bar: 50 μm in (B) and 100 μm in (I and J). For (E and G), different shades of gray represent individual Ctrl hiPSC lines. Different shades of cyan represent individual TS hiPSC lines.

Please cite this article in press as: Birey et al., Dissecting the molecular basis of human interneuron migration in forebrain assembloids from Timothy syndrome, Cell Stem Cell (2021), https://doi.org/10.1016/j.stem.2021.11.011

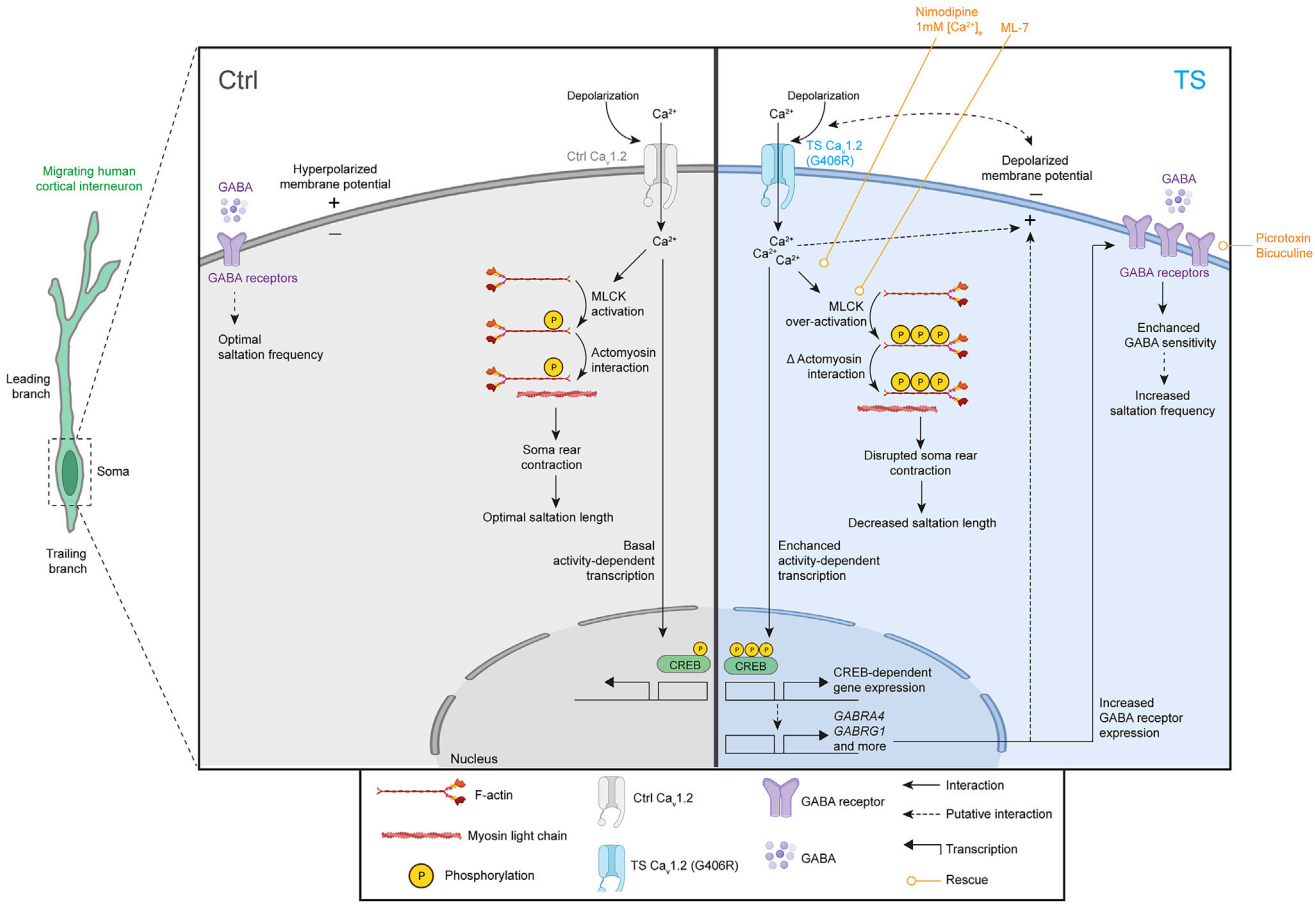

Figure 7. Working model of interneuron migration dysfunction in TS

(Dogterom and Koenderink, 2019). In the neuronal growth cone, actomyosin contractility is tightly coupled to microtubule assembly and disassembly to promote efficient turning and outgrowth (Coles and Bradke, 2015). We find that abnormal calcium influx mediated by TS $Ca_v1.2$ disrupts the coupling between pulling and pushing forces during nucleokinesis. This is possibly related to excess phosphorylation of MLC in the cell soma and aberrant cell-rear contractility, ultimately resulting in decreased saltation length. Additional aspects of intracellular calcium signaling might also contribute to the phenotype. Calcium-induced calcium release (CICR), where calcium from internal stores is released in response to calcium influx (Roderick et al., 2003), is critical in controlling repulsion/attraction in the growth cone (Gasperini et al., 2017). Aberrant CICR, ER calcium handling and/or altered physical interactions with ER-bound receptors could also play roles in the cell-rear contractility defect in TS.

Remarkably, we found that acute modulation of either LTCCs (Nim, low $[Ca^{2+}]_e$, FPL 64176) or downstream cytoskeletal elements (ML-7) increases the saltation length but has no effect on the saltation frequency in TS interneurons. This prompted us to explore alternative pathways that could instead underlie the saltation frequency phenotype. Intracellular calcium entry through $Ca_v1.2$ induces activity-dependent gene expression changes in a cell-type-specific manner (Greenberg et al., 1986; Morgan and Curran, 1986; Murphy et al., 1991). The TS $Ca_v1.2$ channel has been previously shown to cause changes in activity-dependent gene expression programs (Paşca et al., 2011; Tian et al., 2014; Servili et al., 2020). In line with this, we observed enhanced phospho-CREB levels in TS interneurons. The expression of GABA receptors has previously been shown to be regulated by LTCC activity (Saliba et al., 2009), CREB (Yu et al., 2017), and activity-dependent pathways (Roberts et al., 2005), suggesting that their upregulation in TS interneurons may follow $Ca_v1.2$ channel gain of function.

What could cause the RMP changes in TS interneurons? Our RNA sequencing studies in hSS point to global gene expression changes related to electrophysiological properties. In line with this, patch clamping experiments revealed a hSS-specific depolarized RMP phenotype. The transcriptomic analysis identified *KCNC3*, which encodes the voltage-sensitive potassium channel $K_v3.3$, as robustly upregulated in TS hSS. $K_v3.3$ channels drive the repolarization phase of action potentials and are highly expressed in high-spiking neurons (Kaczmarek and Zhang, 2017). Futures studies will be needed to elucidate if this upregulation represents an adaptation to or is a driver of RMP modulation in TS.

GABA, GABA-A receptor activation, and changes in excitability of interneurons have been associated with migration (Cuzon et al., 2006; Heck et al., 2007). In development, GABA can depolarize neurons leading to calcium transients

(Bortone and Polleux, 2009). We found that migrating TS interneurons had relatively depolarized membrane potentials, increased calcium transients, enhanced calcium influx in response to GABA, and larger GABA currents. Moreover, we found that blocking GABA-A receptors decreased the saltation frequency phenotype but left the saltation length unchanged. Together, these data suggest a model in which ambient GABA acts in a paracrine/autocrine fashion in migrating interneurons and provides a pro-migratory signal; in TS, GABA sensitivity is enhanced due to altered transcriptional programs in GABAergic transmission and excitability, leading to increased saltation frequency.

TS patients often present with recurrent seizures (Splawski et al., 2004), which could be linked to hyperexcitable cortical networks. In this study, we describe hypersynchronous activity in TS hCS networks, which is exacerbated by cortical interneuron migration. The excitatory role of GABA is essential for the development of cortical networks (Obrietan et al., 2002; Cancedda et al., 2007). Therefore, it is conceivable that a depolarized RMP and an increased activity of interneurons could exacerbate GABA-induced excitation of TS cortical networks. However, it is important to note that extrapolating *in vitro* findings to complex multi-circuit-level phenomena, such as seizures, is challenging.

Moving forward, several questions remain to be explored. For example, does the TS $Ca_v1.2$ channel directly induce upregulation of GABA receptors via calcium-mediated transcriptional programs, or is it an indirect consequence of electrical changes membrane potential or other homeostatic mechanisms in TS? Do other neurotransmitters secreted by interneurons also play a role in the TS migration phenotype? Glycine, for example, has previously been shown to fine-tune actomyosin contractility in migrating interneurons (Avila et al., 2013). In summary, our work provides novel insights into LTCC-mediated regulation of human cortical interneuron development in the context of disease and suggest strategies for restoring associated defects.

Limitations of the study

Future studies that include additional cells, at multiple stages of *in vitro* differentiation, and hiPSC lines from more individuals (including those carrying non-typical TS mutations) should verify if pharmacological rescue is complete. We found that the effect of GABA-A blockers on saltation frequency was not as robust as the effect of Nim and ML-7 on saltation length. This could be due to the compensatory action of metabotropic GABA-B receptors (Booker et al., 2020) and other cell non-autonomous mechanisms (e.g., glutamate release in cortical network activity). We did not detect changes in transcriptional maturation programs in TS interneurons, but a comprehensive set of functional analyses on interneurons following their migration and integration into cortical networks may reveal electrophysiological dysmaturation phenotypes. Lastly, although we described impaired migration in TS cortical interneurons, it remains to be confirmed through postmortem studies that the number of interneurons is indeed reduced in the cerebral cortex of TS patients. However, assessing absolute numbers of migrated interneurons is not trivial, as cortical interneuron migration is prolonged (continues up to the second year in humans) (Paredes et al., 2016), involves multiple subpallial niches, and is followed by selective apoptosis in the cerebral cortex (Wong and Marín, 2019).

STAR★METHODS

Detailed methods are provided in the online version of this paper and include the following:

- KEY RESOURCES TABLE
- RESOURCE AVAILABILITY
  - Lead contact
  - Materials availability
  - Data and code availability
- EXPERIMENTAL MODEL AND SUBJECT DETAILS
  - Characterization and maintenance of hiPSCs
- METHOD DETAILS
  - Differentiation and assembly of hCS and hSS
  - Human primary tissue
  - hSS dissociation for monolayer culture
  - Real-time qPCR
  - Viral labeling of hSS
  - Fluorescence activated cell sorting (FACS)
  - Activity-dependent gene expression assay
  - Immunofluorescence staining and quantification
  - Migration imaging and analysis
  - Calcium imaging
  - Western blotting
  - Whole-cell patch clamping
  - RNA sequencing
  - Statistics

SUPPLEMENTAL INFORMATION

Supplemental information can be found online at https://doi.org/10.1016/j.stem.2021.11.011.

ACKNOWLEDGMENTS

We thank the members of the Pașca lab, in particular J. Andersen, R.M. Agoglia, N. Thom, S. Kanton, and T. Khan, for insightful discussions, advice, and support. This work was supported by National Institute of Mental Health (R01 MH115012 to S.P.P. and K99 MH119319 to F.B., respectively), National Institute of Mental Health Convergent Neuroscience Consortium (U01 MH115745 to D.H.G. and S.P.P.), the Stanford Human Brain Organogenesis Program in the Wu Tsai Neuroscience Institute (to S.P.P.), the Kwan Funds (to S.P.P.), the Senkut Research Fund (to S.P.P.), the Stanford Maternal & Child Health Research Institute (MCHRI) Postdoctoral Fellowship (to F.B. and O.R.), the American Epilepsy Society Postdoctoral Research Fellowship (to F.B.), the Stanford Science Fellows Program (to A.M.V.), the Autism Science Foundation (ASF), and the Brain and Behavior Research Foundation (BBRF) Young Investigator award (to A.G.). S.P.P. is a New York Stem Cell Foundation (NYSCF) Robertson Stem Cell Investigator and a Chan Zuckerberg Initiative (CZI) Ben Barres Investigator.

AUTHOR CONTRIBUTIONS

F.B. and S.P.P. conceived the project and designed experiments. F.B. and M.V.T. performed hCS and hSS differentiations. F.B. generated forebrain assembloids and performed migration and calcium imaging experiments and analyses. F.B. implemented the DeepLabCut pipeline and downstream analyses. F.B. and M.V.T. performed migration tracking analyses, immunofluorescence stainings, and quantifications. M.V.T. performed the RNA extractions and qPCRs. M.-Y.L. conducted and analyzed electrophysiology experiments. A.G. and D.H.G. analyzed and interpreted the RNA sequencing experiments. M.V.T. and A.M.V. conducted and analyzed western blotting experiments. O.R. developed MATLAB code for calcium transient detection and provided input for the development of other MATLAB routines and electrophysiology

experiments. A.M.P. assisted with primary tissue preparations. F.B. wrote the manuscript with input from all authors. S.P.P. supervised all aspects of the work.

DECLARATION OF INTERESTS

Stanford University holds patents and has provisional patent applications covering the generation of brain region-specific organoids and assembloids (F.B., A.M.P., and S.P.P.).

Received: June 3, 2021
Revised: October 19, 2021
Accepted: November 24, 2021
Published: January 5, 2022

REFERENCES

Anderson, S.A., Eisenstat, D.D., Shi, L., and Rubenstein, J.L.R. (1997). Interneuron migration from basal forebrain to neocortex: dependence on Dlx genes. Science *278*, 474–476.

Avila, A., Vidal, P.M., Dear, T.N., Harvey, R.J., Rigo, J.-M., and Nguyen, L. (2013). Glycine receptor α2 subunit activation promotes cortical interneuron migration. Cell Rep *4*, 738–750.

Barreto-Chang, O.L., and Dolmetsch, R.E. (2009). Calcium imaging of cortical neurons using Fura-2. AM. J. Vis. Exp. *23*, e1067.

Bates, E. (2015). Ion channels in development and cancer. Annu. Rev. Cell Dev. Biol. *31*, 231–247.

Bellion, A., Baudoin, J.-P., Alvarez, C., Bornens, M., and Métin, C. (2005). Nucleokinesis in tangentially migrating neurons comprises two alternating phases: forward migration of the Golgi/centrosome associated with centrosome splitting and myosin contraction at the rear. J. Neurosci. *25*, 5691–5699.

Bers, D.M. (2002). Cardiac excitation-contraction coupling. Nature *415*, 198–205.

Bhat, S., Dao, D.T., Terrillion, C.E., Arad, M., Smith, R.J., Soldatov, N.M., and Gould, T.D. (2012). *CACNA1C* (Cav1.2) in the pathophysiology of psychiatric disease. Prog. Neurobiol. *99*, 1–14.

Birey, F., Andersen, J., Makinson, C.D., Islam, S., Wei, W., Huber, N., Fan, H.C., Metzler, K.R.C., Panagiotakos, G., Thom, N., et al. (2017). Assembly of functionally integrated human forebrain spheroids. Nature *545*, 54–59.

Booker, S.A., Harada, H., Elgueta, C., Bank, J., Bartos, M., Kulik, A., and Vida, I. (2020). Presynaptic GABAB receptors functionally uncouple somatostatin interneurons from the active hippocampal network. eLife *9*, e51156.

Bortone, D., and Polleux, F. (2009). KCC2 expression promotes the termination of cortical interneuron migration in a voltage-sensitive calcium-dependent manner. Neuron *62*, 53–71.

Boulting, G.L., Durresi, E., Ataman, B., Sherman, M.A., Mei, K., Harmin, D.A., Carter, A.C., Hochbaum, D.R., Granger, A.J., Engreitz, J.M., et al. (2021). Activity-dependent regulome of human GABAergic neurons reveals new patterns of gene regulation and neurological disease heritability. Nat. Neurosci. *24*, 437–448.

Buchsbaum, I.Y., and Cappello, S. (2019). Neuronal migration in the CNS during development and disease: insights from *in vivo* and *in vitro* models. Development *146*, dev163766.

Cancedda, L., Fiumelli, H., Chen, K., and Poo, M.-M. (2007). Excitatory GABA action is essential for morphological maturation of cortical neurons *in vivo*. J. Neurosci. *27*, 5224–5235.

Coles, C.H., and Bradke, F. (2015). Coordinating neuronal actin-microtubule dynamics. Curr. Biol. *25*, R677–R691.

Cuzon, V.C., Yeh, P.W., Cheng, Q., and Yeh, H.H. (2006). Ambient GABA promotes cortical entry of tangentially migrating cells derived from the medial ganglionic eminence. Cereb. Cortex *16*, 1377–1388.

Demontis, D., Walters, R.K., Martin, J., Mattheisen, M., Als, T.D., Agerbo, E., Baldursson, G., Belliveau, R., Bybjerg-Grauholm, J., Bækvad-Hansen, M., et al. (2019). Discovery of the first genome-wide significant risk loci for attention deficit/hyperactivity disorder. Nat. Genet. *51*, 63–75.

Dobin, A., Davis, C.A., Schlesinger, F., Drenkow, J., Zaleski, C., Jha, S., Batut, P., Chaisson, M., and Gingeras, T.R. (2013). STAR: ultrafast universal RNA-sequencing aligner. Bioinformatics *29*, 15–21.

Dogterom, M., and Koenderink, G.H. (2019). Actin-microtubule crosstalk in cell biology. Nat. Rev. Mol. Cell Biol. *20*, 38–54.

Dolmetsch, R. (2003). Excitation-transcription coupling: signaling by ion channels to the nucleus. Sci. STKE 2003, PE4.

Finucane, H.K., Bulik-Sullivan, B., Gusev, A., Trynka, G., Reshef, Y., Loh, P.-R., Anttila, V., Xu, H., Zang, C., Farh, K., et al. (2015). Partitioning heritability by functional annotation using genome-wide association summary statistics. Nat. Genet. *47*, 1228–1235.

Gasperini, R.J., Pavez, M., Thompson, A.C., Mitchell, C.B., Hardy, H., Young, K.M., Chilton, J.K., and Foa, L. (2017). How does calcium interact with the cytoskeleton to regulate growth cone motility during axon pathfinding? Mol. Cell. Neurosci. *84*, 29–35.

Greenberg, M.E., Ziff, E.B., and Greene, L.A. (1986). Stimulation of neuronal acetylcholine receptors induces rapid gene transcription. Science *234*, 80–83.

Grove, J., Ripke, S., Als, T.D., Mattheisen, M., Walters, R.K., Won, H., Pallesen, J., Agerbo, E., Andreassen, O.A., Anney, R., et al. (2019). Identification of common genetic risk variants for autism spectrum disorder. Nat. Genet. *51*, 431–444.

Heck, N., Kilb, W., Reiprich, P., Kubota, H., Furukawa, T., Fukuda, A., and Luhmann, H.J. (2007). GABA-A receptors regulate neocortical neuronal migration *in vitro* and *in vivo*. Cereb. Cortex *17*, 138–148.

Hodge, R.D., Bakken, T.E., Miller, J.A., Smith, K.A., Barkan, E.R., Graybuck, L.T., Close, J.L., Long, B., Johansen, N., Penn, O., et al. (2019). Conserved cell types with divergent features in human versus mouse cortex. Nature *573*, 61–68.

Howard, D.M., Adams, M.J., Clarke, T.-K., Hafferty, J.D., Gibson, J., Shirali, M., Coleman, J.R.I., Hagenaars, S.P., Ward, J., Wigmore, E.M., et al. (2019). Genome-wide meta-analysis of depression identifies 102 independent variants and highlights the importance of the prefrontal brain regions. Nat. Neurosci. *22*, 343–352.

Inamura, N., Kimura, T., Tada, S., Kurahashi, T., Yanagida, M., Yanagawa, Y., Ikenaka, K., and Murakami, F. (2012). Intrinsic and extrinsic mechanisms control the termination of cortical interneuron migration. J. Neurosci. *32*, 6032–6042.

Kaczmarek, L.K., and Zhang, Y. (2017). Kv3 channels: enablers of rapid firing, neurotransmitter release, and neuronal endurance. Physiol. Rev. *97*, 1431–1468.

Kamijo, S., Ishii, Y., Horigane, S.-I., Suzuki, K., Ohkura, M., Nakai, J., Fujii, H., Takemoto-Kimura, S., and Bito, H. (2018). A critical neurodevelopmental role for L-type voltage-gated calcium channels in neurite extension and radial migration. J. Neurosci. *38*, 5551–5566.

Khan, T.A., Revah, O., Gordon, A., Yoon, S.-J., Krawisz, A.K., Goold, C., Sun, Y., Kim, C.H., Tian, Y., Li, M.-Y., et al. (2020). Neuronal defects in a human cellular model of 22q11.2 deletion syndrome. Nat. Med. *26*, 1888–1898.

Korotkevich, G., Sukhov, V., Budin, N., Shpak, B., Artyomov, M.N., and Sergushichev, A. (2021). Fast gene set enrichment analysis (bioRxiv). bioRxiv. https://doi.org/10.1101/060012.

Krey, J.F., Paşca, S.P., Shcheglovitov, A., Yazawa, M., Schwemberger, R., Rasmusson, R., and Dolmetsch, R.E. (2013). Timothy syndrome is associated with activity-dependent dendritic retraction in rodent and human neurons. Nat. Neurosci. *16*, 201–209.

Krienen, F.M., Goldman, M., Zhang, Q., C.H. del Rosario, R., Florio, M., Machold, R., Saunders, A., Levandowski, K., Zaniewski, H., Schuman, B., et al. (2020). Innovations present in the primate interneuron repertoire. Nature *586*, 262–269.

Kuo, I.Y., and Ehrlich, B.E. (2015). Signaling in muscle contraction. Cold Spring Harb. Perspect. Biol. *7*, a006023.

Langfelder, P., and Horvath, S. (2008). WGCNA: an R package for weighted correlation network analysis. BMC Bioinformatics *9*, 559.

Leblond, C.S., Le, T.-L., Malesys, S., Cliquet, F., Tabet, A.-C., Delorme, R., Rolland, T., and Bourgeron, T. (2021). Operative list of genes associated

with autism and neurodevelopmental disorders based on database review. Mol. Cell. Neurosci. *113*, 103623.

Manent, J.-B., Demarque, M., Jorquera, I., Pellegrino, C., Ben-Ari, Y., Aniksztejn, L., and Represa, A. (2005). A noncanonical release of GABA and glutamate modulates neuronal migration. J. Neurosci. *25*, 4755–4765.

Marín, O. (2012). Interneuron dysfunction in psychiatric disorders. Nat. Rev. Neurosci. *13*, 107–120.

Marín, O. (2013). Cellular and molecular mechanisms controlling the migration of neocortical interneurons. Eur. J. Neurosci. *38*, 2019–2029.

Martini, F.J., and Valdeolmillos, M. (2010). Actomyosin contraction at the cell rear drives nuclear translocation in migrating cortical interneurons. J. Neurosci. *30*, 8660–8670.

Maset, A., Galla, L., Francia, S., Cozzolino, O., Capasso, P., Goisis, R.C., Losi, G., Lombardo, A., Ratto, G.M., and Lodovichi, C. (2021). Altered Cl− homeostasis hinders forebrain GABAergic interneuron migration in a mouse model of intellectual disability. Proc. Natl. Acad. Sci. USA *118*, e2016034118.

Mathis, A., Mamidanna, P., Cury, K.M., Abe, T., Murthy, V.N., Mathis, M.W., and Bethge, M. (2018). DeepLabCut: markerless pose estimation of user-defined body parts with deep learning. Nat. Neurosci. *21*, 1281–1289.

Mathis, M.W., and Mathis, A. (2020). Deep learning tools for the measurement of animal behavior in neuroscience. Curr. Opin. Neurobiol. *60*, 1–11.

Mayer, C., Hafemeister, C., Bandler, R.C., Machold, R., Batista Brito, R., Jaglin, X., Allaway, K., Butler, A., Fishell, G., and Satija, R. (2018). Developmental diversification of cortical inhibitory interneurons. Nature *555*, 457–462.

McKenna, A., Hanna, M., Banks, E., Sivachenko, A., Cibulskis, K., Kernytsky, A., Garimella, K., Altshuler, D., Gabriel, S., Daly, M., and DePristo, M.A. (2010). The Genome Analysis Toolkit: a MapReduce framework for analyzing next-generation DNA sequencing data. Genome Res *20*, 1297–1303.

Meechan, D.W., Tucker, E.S., Maynard, T.M., and LaMantia, A.-S. (2012). Cxcr4 regulation of interneuron migration is disrupted in 22q11.2 deletion syndrome. Proc. Natl. Acad. Sci. USA *109*, 18601–18606.

Mi, D., Li, Z., Lim, L., Li, M., Moissidis, M., Yang, Y., Gao, T., Hu, T.X., Pratt, T., Price, D.J., et al. (2018). Early emergence of cortical interneuron diversity in the mouse embryo. Science *360*, 81–85.

Miura, Y., Li, M.-Y., Birey, F., Ikeda, K., Revah, O., Thete, M.V., Park, J.-Y., Puno, A., Lee, S.H., Porteus, M.H., and Pașca, S.P. (2020). Generation of human striatal organoids and cortico-striatal assembloids from human pluripotent stem cells. Nat. Biotechnol. *38*, 1421–1430.

Morgan, J.I., and Curran, T. (1986). Role of ion flux in the control of c-*fos* expression. Nature *322*, 552–555.

Mullins, N., Forstner, A.J., O'Connell, K.S., Coombes, B., Coleman, J.R.I., Qiao, Z., Als, T.D., Bigdeli, T.B., Børte, S., Bryois, J., et al. (2020). Genome-wide association study of over 40,000 bipolar disorder cases provides novel biological insights. medRxiv. medRxiv. https://doi.org/10.1101/2020.09.17.20187054.

Muraki, K., and Tanigaki, K. (2015). Neuronal migration abnormalities and its possible implications for schizophrenia. Front. Neurosci. *9*, 74.

Murphy, T.H., Worley, P.F., and Baraban, J.M. (1991). L-type voltage-sensitive calcium channels mediate synaptic activation of immediate early genes. Neuron *7*, 625–635.

Obrietan, K., Gao, X.-B., and van den Pol, A.N. (2002). Excitatory actions of GABA increase BDNF expression via a MAPK-CREB-dependent mechanism—a positive feedback circuit in developing neurons. J. Neurophysiol. *88*, 1005–1015.

Panagiotakos, G., Haveles, C., Arjun, A., Petrova, R., Rana, A., Portmann, T., Paşca, S.P., Palmer, T.D., and Dolmetsch, R.E. (2019). Aberrant calcium channel splicing drives defects in cortical differentiation in Timothy syndrome. eLife *8*, e51037.

Pardiñas, A.F., Holmans, P., Pocklington, A.J., Escott-Price, V., Ripke, S., Carrera, N., Legge, S.E., Bishop, S., Cameron, D., Hamshere, M.L., et al. (2018). Common schizophrenia alleles are enriched in mutation-intolerant genes and in regions under strong background selection. Nat. Genet. *50*, 381–389.

Paredes, M.F., James, D., Gil-Perotin, S., Kim, H., Cotter, J.A., Ng, C., Sandoval, K., Rowitch, D.H., Xu, D., McQuillen, P.S., et al. (2016). Extensive migration of young neurons into the infant human frontal lobe. Science *354*, aaf7073.

Parikshak, N.N., Gandal, M.J., and Geschwind, D.H. (2015). Systems biology and gene networks in neurodevelopmental and neurodegenerative disorders. Nat. Rev. Genet. *16*, 441–458.

Paşca, S.P., Portmann, T., Voineagu, I., Yazawa, M., Shcheglovitov, A., Paşca, A.M., Cord, B., Palmer, T.D., Chikahisa, S., Nishino, S., et al. (2011). Using iPSC-derived neurons to uncover cellular phenotypes associated with Timothy syndrome. Nat. Med. *17*, 1657–1662.

Powell, E.M. (2013). Interneuron development and epilepsy: early genetic defects cause long-term consequences in seizures and susceptibility. Epilepsy Curr *13*, 172–176.

Purcell, S., Neale, B., Todd-Brown, K., Thomas, L., Ferreira, M.A.R., Bender, D., Maller, J., Sklar, P., de Bakker, P.I.W., Daly, M.J., and Sham, P.C. (2007). PLINK: a tool set for whole-genome association and population-based linkage analyses. Am. J. Hum. Genet. *81*, 559–575.

Purcell, S.M., Moran, J.L., Fromer, M., Ruderfer, D., Solovieff, N., Roussos, P., O'Dushlaine, C., Chambert, K., Bergen, S.E., Kähler, A., et al. (2014). A polygenic burden of rare disruptive mutations in schizophrenia. Nature *506*, 185–190.

Ripke, S., Neale, B.M., Corvin, A., Walters, J.T.R., Farh, K.-H., Holmans, P.A., Lee, P., Bulik-Sullivan, B., Collier, D.A., Huang, H., et al. (2014). Biological insights from 108 schizophrenia-associated genetic loci. Nature *511*, 421–427.

Ritchie, M.E., Phipson, B., Wu, D., Hu, Y., Law, C.W., Shi, W., and Smyth, G.K. (2015). *limma* powers differential expression analyses for RNA-sequencing and microarray studies. Nucleic Acids Res *43*, e47.

Roberts, D.S., Raol, Y.H., Bandyopadhyay, S., Lund, I.V., Budreck, E.C., Passini, M.A., Wolfe, J.H., Brooks-Kayal, A.R., and Russek, S.J. (2005). Egr3 stimulation of GABRA4 promoter activity as a mechanism for seizure-induced up-regulation of GABA(A) receptor alpha4 subunit expression. Proc. Natl. Acad. Sci. USA *102*, 11894–11899.

Robinson, M.D., McCarthy, D.J., and Smyth, G.K. (2010). edgeR: a Bioconductor package for differential expression analysis of digital gene expression data. Bioinformatics *26*, 139–140.

Roderick, H.L., Berridge, M.J., and Bootman, M.D. (2003). Calcium-induced calcium release. Curr. Biol. *13*, R425.

Saliba, R.S., Gu, Z., Yan, Z., and Moss, S.J. (2009). Blocking L-type voltage-gated Ca2+ channels with dihydropyridines reduces γ-aminobutyric acid type A receptor expression and synaptic inhibition. J. Biol. Chem. *284*, 32544–32550.

Schaar, B.T., and McConnell, S.K. (2005). Cytoskeletal coordination during neuronal migration. Proc. Natl. Acad. Sci. USA *102*, 13652–13657.

Schindelin, J., Arganda-Carreras, I., Frise, E., Kaynig, V., Longair, M., Pietzsch, T., Preibisch, S., Rueden, C., Saalfeld, S., Schmid, B., et al. (2012). Fiji: an open-source platform for biological-image analysis. Nat. Methods *9*, 676–682.

Servili, E., Trus, M., Sajman, J., Sherman, E., and Atlas, D. (2020). Elevated basal transcription can underlie timothy channel association with autism related disorders. Prog. Neurobiol. *191*, 101820.

Silbereis, J.C., Pochareddy, S., Zhu, Y., Li, M., and Sestan, N. (2016). The cellular and molecular landscapes of the developing human central nervous system. Neuron *89*, 248–268.

Silva, C.G., Peyre, E., and Nguyen, L. (2019). Cell migration promotes dynamic cellular interactions to control cerebral cortex morphogenesis. Nat. Rev. Neurosci. *20*, 318–329.

Sloan, S.A., Andersen, J., Paşca, A.M., Birey, F., and Paşca, S.P. (2018). Generation and assembly of human brain region-specific three-dimensional cultures. Nat. Protoc. *13*, 2062–2085.

Splawski, I., Timothy, K.W., Sharpe, L.M., Decher, N., Kumar, P., Bloise, R., Napolitano, C., Schwartz, P.J., Joseph, R.M., Condouris, K., et al. (2004). Ca(V)1.2 calcium channel dysfunction causes a multisystem disorder including arrhythmia and autism. Cell *119*, 19–31.

Tan, J.L., Ravid, S., and Spudich, J.A. (1992). Control of nonmuscle myosins by phosphorylation. Annu. Rev. Biochem. *61*, 721–759.

Tian, Y., Voineagu, I., Paşca, S.P., Won, H., Chandran, V., Horvath, S., Dolmetsch, R.E., and Geschwind, D.H. (2014). Alteration in basal and depolarization induced transcriptional network in iPSC derived neurons from Timothy syndrome. Genome Med *6*, 75.

Voineagu, I., Wang, X., Johnston, P., Lowe, J.K., Tian, Y., Horvath, S., Mill, J., Cantor, R.M., Blencowe, B.J., and Geschwind, D.H. (2011). Transcriptomic analysis of autistic brain reveals convergent molecular pathology. Nature *474*, 380–384.

Wamsley, B., and Fishell, G. (2017). Genetic and activity-dependent mechanisms underlying interneuron diversity. Nat. Rev. Neurosci. *18*, 299–309.

Wheeler, D.G., Groth, R.D., Ma, H., Barrett, C.F., Owen, S.F., Safa, P., and Tsien, R.W. (2012). CaV1 and CaV2 channels engage distinct modes of Ca2+ signaling to control CREB-dependent gene expression. Cell *149*, 1112–1124.

Wong, F.K., and Marín, O. (2019). Developmental cell death in the cerebral cortex. Annu. Rev. Cell Dev. Biol. *35*, 523–542.

Yap, E.-L., and Greenberg, M.E. (2018). Activity-regulated transcription: bridging the gap between neural activity and behavior. Neuron *100*, 330–348.

Yoon, S.-J., Elahi, L.S., Paşca, A.M., Marton, R.M., Gordon, A., Revah, O., Miura, Y., Walczak, E.M., Holdgate, G.M., Fan, H.C., et al. (2019). Reliability of human cortical organoid generation. Nat. Methods *16*, 75–78.

Yu, G., Wang, L.-G., Han, Y., and He, Q.-Y. (2012). clusterProfiler: an R package for comparing biological themes among gene clusters. OMICS J. Integr. Biol. *16*, 284–287.

Yu, J., Liu, Z., Wang, L., Wu, G., and Wu, M. (2017). Increased GABA (A) receptors alpha1, gamma2, delta subunits might be associated with the activation of the CREB gene in low Mg2+ model of epilepsy. Neuropsychiatry *07*, 398–405.

Zhang, B., and Horvath, S. (2005). A general framework for weighted gene co-expression network analysis. Stat. Appl. Genet. Mol. Biol. *4*, 17.

Please cite this article in press as: Birey et al., Dissecting the molecular basis of human interneuron migration in forebrain assembloids from Timothy syndrome, Cell Stem Cell (2021), https://doi.org/10.1016/j.stem.2021.11.011

STAR★METHODS

KEY RESOURCES TABLE

REAGENT or RESOURCE	SOURCE	IDENTIFIER
Antibodies		
Mouse monoclonal anti-Cav1.2, conjugated to DyLight 488	StressMarq Biosciences	Cat# SMC-300D-DY488
Rabbit polyclonal anti-phospho-CREB (Ser133)	Millipore Sigma	Cat# 06-519
Rabbit polyclonal anti-phospho-Myosin Light Chain 2 (Ser19)	Cell Signaling	Cat# 3671S
Rabbit IgG anti-Myosin Light Chain 2 (D18E2)	Cell Signaling	Cat# 8505S
Guinea pig polyclonal anti-MAP2	Synaptic Systems	Cat# 188 004
Chicken polyclonal anti-GFP	GeneTex	Cat# GTX13970
Mouse monoclonal anti-beta Tubulin B3 (TUJ1)	Biolegend	Cat# 801202
Rabbit polyclonal anti-GABA antibody	Sigma	Cat# A2052
Rabbit polyclonal anti-Calretinin	Swant	Cat# 7697
Guinea pig polyclonal anti-Calbindin D28K	Synaptic Systems	Cat# 214 005
Rat monoclonal anti-Somatostatin (SST)	Millipore Sigma	Cat# MAB354
Mouse monoclonal anti-beta Actin	Sigma Aldrich	Cat# A5316
Bacterial and virus strains		
LV-Dlxi1/2b-eGFP	Gift from J.Rubenstein	N/A
AAV-DJ-Dlx5/6-eGFP	Addgene	83900
AAV-DJ-Dlxi1/2b-mScarlet-P2A-GCaMP6s	VectorBuilder	N/A
AAV-DJ-Dlx5/6-GCaMP6f	Addgene	83899
AAV-DJ-hSyn1-eYFP	Stanford Gene Vector and Virus Core	N/A
AAV-DJ-hSyn1-GCaMP6s	Stanford Gene Vector and Virus Core	N/A
AAV1-hSyn1-jGCaMP7s	Addgene	104487-AAV1
Chemicals, peptides, and recombinant proteins		
B-27 supplement without vitamin A	Life Technologies	Cat# 12587010
N-2 supplement	Life Technologies	Cat# 17502048
Human recombinant FGF-2	R&D Systems	Cat# 233-FB
Human recombinant EGF	R&D Systems	Cat# 236-EG
Human recombinant BDNF	Peprotech	Cat# 450-02
Human recombinant NT3	Peprotech	Cat# 450-03
Dorsomorphin	Sigma-Aldrich	Cat# P5499
SB-431542	Tocris	Cat# 1614
SAG	Millipore	Cat# 566660
IWP2	STEMCELL Technologies	Cat# 72124
Nimodipine	Tocris	Cat# 0600
ML-7	Tocris	Cat# 4310
Isradipine	Tocris	Cat# 2004
FPL 64176	Tocris	Cat# 1403
GABA	Tocris	Cat# 0344
NBQX	Tocris	Cat# 0373
D-AP5 (APV)	Tocris	Cat# 0106
Tetrodotoxin citrate (TTX)	Tocris	Cat# 1069
Picrotoxin	Tocris	Cat# 1128
Bicuculine	Tocris	Cat# 0131

(*Continued on next page*)

Please cite this article in press as: Birey et al., Dissecting the molecular basis of human interneuron migration in forebrain assembloids from Timothy syndrome, Cell Stem Cell (2021), https://doi.org/10.1016/j.stem.2021.11.011

Continued

REAGENT or RESOURCE	SOURCE	IDENTIFIER
Critical commercial assays		
Quick-RNA Miniprep kit	Zymo Research	Cat# R1054
NEBNext Ultra™ II RNA Library Prep Kit	NEB	Cat# E7770S
Deposited data		
RNA-sequencing data	This study	GEO: GSE175898
Experimental models: Cell lines		
hiPSC lines used in the study is listed in Table S1		N/A
Oligonucleotides		
Primers used in the study is listed in Table S1		N/A
Software and algorithms		
ImageJ (Fiji)	Schindelin et al., 2012	https://imagej.net/Fiji
MATLAB vR2019b, v9.4.0	MathWorks	https://www.mathworks.com/help/matlab/ref/rand.html
Python v3.6.9	Python	https://www.python.org/
R v4.0.5 and 4.1.0	R	https://www.r-project.org/
DeepLabCut, v2.1.6	Mathis et al., 2018	https://github.com/DeepLabCut/DeepLabCut/blob/master/README.md
STAR v2.5.2b	Dobin et al., 2013	http://code.google.com/p/rna-star/
PLINK v1.09	Purcell et al., 2007	https://zzz.bwh.harvard.edu/plink/
GATK Haplotype caller v3.3	McKenna et al., 2010	https://gatk.broadinstitute.org/hc/en-us/articles/360037225632-HaplotypeCaller
edgeR	Robinson et al., 2010	https://bioconductor.org/packages/release/bioc/html/edgeR.html
Limma	Ritchie et al., 2015	https://bioconductor.org/packages/release/bioc/html/limma.html
Fgsea v1.10.1	Korotkevich et al., 2021	http://bioconductor.org/packages/release/bioc/html/fgsea.html
Ggplot2 v3.3.3	N/A	https://cran.r-project.org/web/packages/ggplot2/index.html
WGCNA v1.68	Langfelder and Horvath, 2008	https://horvath.genetics.ucla.edu/html/CoexpressionNetwork/Rpackages/WGCNA/
cluterProfiler v3.12.0	Yu et al., 2012	https://bioconductor.org/packages/release/bioc/html/clusterProfiler.html
LDscore regression v1.0.0	Finucane et al., 2015	https://github.com/bulik/ldsc
DaVinci Resolve 16	Blackmagic Design	https://www.blackmagicdesign.com/products/davinciresolve/
Prism v8.4.2-9.0.0	Graphpad	https://www.graphpad.com/
Other		
10 cm ultralow attachment plates	Corning	Cat# 3262
24-well ultralow attachment plates	Corning	Cat# 3473
Cell culture inserts, 0.4 μm pore size	Corning	Cat# 353090
Glass-bottom 96-well plate #1.5 cover glass	Cellvis	Cat# P96-1.5H-N
Glass-bottom 6-well plate #1.5 cover glass	Cellvis	Cat# P06-1.5H-N

RESOURCE AVAILABILITY

Lead contact

Further information and requests for resources and reagents should be directed to and will be fulfilled by the lead contact, Dr. Sergiu P. Pasca (spasca@stanford.edu).

Materials availability

This study did not generate new unique reagents.

Data and code availability

RNA sequencing data have been deposited at GEO and are publicly available (GEO: GSE175898). Any additional information required to reanalyze the data reported in this paper, including custom-written MATLAB and R routines, is available from the lead contact upon request.

EXPERIMENTAL MODEL AND SUBJECT DETAILS

Characterization and maintenance of hiPSCs

hiPSC lines used in this study were validated using standardized methods as previously described (Paşca et al., 2011; Birey et al., 2017). Cultures were frequently tested for Mycoplasma and maintained free of Mycoplasma. A total of 8 Ctrl hiPSC lines derived from fibroblasts collected from 8 healthy individuals and 3 hiPS cell lines derived from fibroblasts collected from 3 individuals with TS were used for experiments (Table S1). Approval was obtained from the Stanford IRB panel, and informed consent was obtained from all participants.

METHOD DETAILS

Differentiation and assembly of hCS and hSS

hCS and hSS differentiations from hiPSCs grown on mouse embryonic fibroblast (MEF) feeder layers were performed as previously described (Birey et al., 2017; Sloan et al., 2018). For hCS and hSS differentiations from feeder-free maintained hiPSCs, cells were maintained on vitronectin-coated plates (5 μg/mL, Thermo Fisher Scientific, A14700) in Essential 8 (E8) medium (Thermo Fisher Scientific, A1517001). Cells were passaged every 4-5 days with UltraPure 0.5 mM EDTA, pH 8.0 (Thermo Fisher Scientific, 15575020). Two days prior to aggregation, hiPSCs were exposed to 1% DMSO (Sigma-Aldrich, 472301) in E8 medium. For the generation of 3D neural spheroids, hiPSCs were incubated with Accutase (Innovative Cell Technologies, AT104) at 37 °C for 7 minutes and then single-cell dissociated. For aggregation into spheroids, 2.5-3 × 10^6 single cells were added per AggreWell 800 plate well in E8 medium supplemented with the ROCK inhibitor Y27632 (10 μM, Selleck Chemicals, S1049), centrifuged at 100*g* for 3 minutes and then incubated overnight at 37°C with 5% CO_2. Next day, spheroids consisting of approximately 10,000 cells were dislodged from each microwell by pipetting the E8 medium up and down in the well with a P1000 pipette with a cut tip and transferred into ultra-low attachment plastic dishes (Corning, 3262) in Essential 6 (E6) medium (Thermo Fisher Scientific, A1516401) supplemented with the SMAD pathway inhibitors dorsomorphin (2.5 μM, Sigma-Aldrich, P5499) and SB-431542 (10 μM, R&D Systems, 1614). Feeder-free hCS differentiation was performed as previously described (Yoon et al., 2019) using the recipe variant without XAV299. Feeder-free hSS differentiation protocol was based on the Feeder-free hCS differentiation protocol with the following modifications (added on top of small molecules/growth factors specified in the hCS recipe): day 3–6; XAV-939 (2.5μM, Tocris, 3748), day 7–24; IWP-2 (2.5μM, Selleck Chemicals, S7085), day 13–24; SAG (100nM, EMD Millipore, 566660). To promote progenitor differentiation in hCS and hSS, BDNF (20 ng/mL) and NT-3 (20 ng/mL) were added starting at day 25 with media changes every other day. After day 43, media changes every 4-5 days were performed only with neural media (NM) without growth factors. Assembly of hCS and hSS to generate forebrain assembloids was performed as previously described (Birey et al., 2017; Sloan et al., 2018).

Human primary tissue

Human brain specimens were obtained under a protocol approved by the Research Compliance Office at Stanford University. PCW18-23 forebrain tissue was processed immediately after arrival.

hSS dissociation for monolayer culture

hSS dissociation for monolayer culture was performed as previously described (Miura et al., 2020) with minor modifications. Briefly, 2–3 randomly selected hSS per hiPSC line were pooled in a 1.5-ml Eppendorf tube in the dissociation solution (10U/mL papain,Worthington Biochemical, LS003119), 1 mM EDTA, 10 mM HEPES (pH 7.4), 100 μg/mL BSA, 5 mM L-cysteine and 500 μg/mL DNase I (Roche, 10104159001). Cells were incubated at 37°C for 20-25 minutes and gently shaken once midway through. Papain was inactivated with 10% FBS in NM, and hSS were then gently triturated with a P1000 pipette. Samples were centrifuged once at 1,200 rpm for 4 minutes, filtered with a 70-μm Flowmi Cell Strainer (Bel-Art, H13680-0070) and then suspended in NM with BDNF (20 ng/mL) and NT-3 (20 ng/mL). 0.75-1 × 10^5 cells were seeded on 15-mm round coverslips (Warber Instruments, 64-0713). Coverslips were coated with approximately 0.001875% polyethylenimine (Sigma-Aldrich, 03880) for 0.5-1 hour at room temperature, washed 3-4 times and air-dried prior to plating. Plated cells were cultured in NM supplemented with BDNF (20 ng/mL) and NT-3 (20 ng/mL) with media changes every other day.

Real-time qPCR

RNA extraction was performed using RNeasy Mini Kit (Qiagen, 74106). Genomic DNA was removed prior to cDNA synthesis using DNase I, Amplification Grade (Thermo Fisher Scientific, 18068-015). Reverse transcription was performed using the SuperScript III First-Strand Synthesis SuperMix for qRT–PCR (Thermo Fisher Scientific, 11752250). qPCR was performed using the SYBR Green PCR Master Mix (Thermo Fisher Scientific, 4312704) with a ViiA7 Real-Time PCR System (Thermo Fisher Scientific, 4453545). Primers used in this experiment are listed in Table S1.

Viral labeling of hSS

hSS were transferred to a 1.5-ml Eppendorf tube containing 200 μl NM and incubated with virus overnight at 37°C with 5% CO_2. The next day, fresh NM (800 μl) was added. The following day, hSS were transferred into fresh culture medium in ultra-low attachment plates (Corning, 3471, 3261). The expression was evident 1–2 weeks after infection across viral reporters used throughout the study.

Fluorescence activated cell sorting (FACS)

hCS and hSS from forebrain assembloids (4-10 assembloids per line, pooled by line) were split with a sterile disposable scalpel and single-cell dissociated as previously described (Birey et al., 2017). $eGFP^+$ interneurons were then sorted from split hCS and hSS separately using gates determined by forward/side scatter and exclusion staining with Hoechst 33258 (Thermo Fisher Scientific, H3569). Cells were collected in PBS with 0.04% BSA, pelleted by spinning them down at 1200 rpm for 7 minutes.

Activity-dependent gene expression assay

hSS were incubated in low-potassium Tyrode's solution (low-KCl; 5 mM KCl: 129 mM NaCl, 2 mM $CaCl_2$, 1 mM $MgCl_2$, 30 mM glucose, 25 mM HEPES, pH 7.4) supplemented either with DMSO (vehicle) or Nim (5μM) for 5 days. On day 4, A subset of hSS in each group was depolarized for 1 hour or 6 hours with high-potassium Tyrode's solution (high-KCl; 67 mM KCl: 67 mM NaCl, 2 mM $CaCl_2$, 1 mM $MgCl_2$, 30 mM glucose and 25 mM HEPES, pH 7.4). RNA extraction, cDNA amplification and qPCR were performed as described above. Primers used in this experiment are listed in Table S1.

Immunofluorescence staining and quantification

hSS were fixed in 4% PFA–PBS for 2 hours at 4°C, washed in PBS once and transferred to 30% sucrose–PBS for 2–3 days. They were next embedded in optimal cutting temperature (OCT) compound (Tissue-Tek OCT Compound 4583, Sakura Finetek) and 30% sucrose–PBS (1:1) for cryosectioning (18-20 μm-thick sections) using a Leica Cryostat (Leica, CM1850). Plated hSS cultures on glass coverslips were fixed in 4% PFA at room temperature for 10 minutes and then rinsed twice for 5 minutes with PBS.

For immunofluorescence staining, cryosections were washed with PBS and blocked in 10% normal donkey serum (NDS; Millipore Sigma, S30-M) and 0.3% Triton X-100 (Millipore Sigma, T9284-100ML) diluted in PBS for 1 hour at room temperature. Sections were then incubated overnight at 4 °C with primary antibodies diluted in PBS containing 10% NDS. PBS was used to wash away excess primary antibodies, and the cryosections were incubated with secondary antibodies in PBS containing 10% NDS for 1 h.The following primary antibodies were used for staining: anti-phospho-CREB (ser133) antibody (1:1000 dilution, rabbit, Millipore Sigma, 06-519), anti-phospho-Myosin Light Chain 2 (Ser19) antibody (1:200 dilution, rabbit, Cell Signaling, 3671S), anti-Myosin Light Chain 2 (D18E2) antibody (1:200 dilution, rabbit, Cell Signaling, 8505S), anti-MAP2 antibody (1:10,000 dilution, guinea pig, Synaptic Systems, 188 004), anti-GFP antibody (1:10,000 dilution, chicken, GeneTex, GTX13970), anti-Beta Tubulin B3 (TUJ1) antibody (1:10,000 dilution, mouse, Biolegend, 801202), anti-GABA antibody (1:1000 dilution, rabbit, Sigma, A2052), anti-Calretinin antibody (1:2000 dilution, rabbit, Swant, 7697), anti-Calbindin D28K antibody (1:1000, guinea pig, Synaptic Systems, 214 005), anti-Somatostatin (SST) antibody (1:200 dilution, rat, Millipore Sigma, MAB354).

For live staining of $Ca_v1.2$, plated hSS cells infected with LV-Dlxi1/2b-mScarlet (Vector Builder) were incubated in Anti-Cav1.2 antibody conjugated with DyLight-488 (1:100, StressMarq Biosciences, SMC-300D-DY488) for 30 minutes, rinsed three times with NM and fixed in 4% PFA at room temperature for 10 minutes.

For fluorescence intensity quantifications, 16-bit confocal images (Leica TCS SP8 confocal microscope) were collected and processed in Fiji (ImageJ, version 2.1.0, NIH) using the same parameters across conditions per experiment. Regions-of-interest (ROIs) were defined using ROI manager in Fiji either by $DAPI^+$ nuclei (pCREBs133 quantifications; Figure S5C) or $MAP2^+$ soma (pMLC2s19 quantifications; Figure 3G) and mean gray values were collected per ROI. Gray values were collected from a cell-absent ROI and subtracted from cell-ROI values for background normalization per field. All values were subsequently normalized to mean Ctrl mean gray value.

For the sphericity quantifications, high-resolution images of $eGFP^+$ interneurons and associated $DAPI^+$ nuclei were 3D-rendered (Imaris, version 9.7.0, Bitplane). The sphericity was calculated as shown in Figure S1H.

Migration imaging and analysis

Live-cell migration analysis and pharmacology were performed as previously described (Birey et al., 2017; Sloan et al., 2018). Briefly, hSS labeled with LV-Dlxi1/2b-eGFP (gift from J. Rubenstein) was assembled with hCS between d60 and d100 to generate forebrain assembloids. Forebrain assembloids 15-45 days after assembly were transferred to a Corning 96-well microplate (Corning, 4580; one assembloid per well) in 200μL NM and incubated in an environmentally controlled chamber (Oko Lab, H201 T Unit-BL with 5% CO_2/air perfusion) for 15–30 minutes before imaging on a Leica TCS SP8 confocal microscope. GFP^+ interneurons from 6-8 assembloids were imaged (10x objective, 0.75x zoom) in a given session at a rate of 18-20 minutes per volume (~200μm volume per assembloid) for 18-22 hours. For pharmacology experiments, following the baseline imaging, half-volume media changes with fresh media containing the drug at twice the working concentration were carefully performed under the hood without disturbing the assembloids and transferred back to the confocal. The fields were adjusted for minor shifts pre-acquisition. For DeepLabCut analysis, high-resolution migration imaging was performed (20x objective, 2-3x zoom) at a rate of approximately 45 seconds per volume for 3-6 hours. For

migration imaging in primary fetal cortical slices, 400μm vibrotome-section cortical slices were placed on culture inserts with 0.4 mm pore size (Corning, 353090), infected with LV-Dlxi1/2-eGFP and imaged 10-14 days after infection. 4-5 fields were imaged per slice (10x objective, 0.75x zoom).

Saltation length and saltation frequency quantifications were performed as previously described (Birey et al., 2017). All migrating interneurons present in a specific field over the entire imaging period were included in the analysis. Given the highly motile nature of interneurons and the relatively shallow imaging depth (~200 μm), a fraction of cells leaves the imaging field during these long-term imaging sessions. These cells cannot, therefore, be included in the analysis. Cells that are immobile either during the baseline or drug imaging windows were also excluded. For primary tissue migration imaging, since the cells are not paired, we included cells that were in the imaging field at least more than 50% of the imaging period to maximize the sample size in these experiments. The migration imaging for DeepLabCut (DLC) analysis was performed at a high spatiotemporal resolution compared to standard migration imaging experiments used for migration pharmacology experiments (standard: 18–20 min per volume; DLC = 45 sec per volume, standard = 10x objective, 0.4 NA, 1x zoom; DLC: 20x objective, 0.75 NA, 2–2.5x zoom). For DeepLabCut analysis, imaging planes were cropped to contain individual saltations from single interneurons. Following drift correction (Linear Stack Alignment plugin) and smoothing (Gaussian Blur 3D plugin) in Fiji, timeseries stacks (250-400 frames in total, 45 seconds per frame) were converted to .avi files in Fiji. DeepLabCut (v2.16, v2.2b6) with GPU support (NVIDIA GeForce GTX 1080 Ti) was installed as per developers' instructions. Config files were edited to label ROIs. 19 training frames that were most distinct across each timeseries was automatically extracted using the k-means algorithm (cluster step = 1, network = resnet_50, augmentation = imgaug) and ROIs were manually annotated in each training frame per video. Network was then trained for up to 100,000 iterations or until the loss plateaued. Network was evaluated and videos were analyzed with filtered predictions. Occasional ROI mismatch was detected by thresholding outlier likelihood measurements and removed by smoothening using moving median function in MATLAB (k= 1000-2000). Tracking fidelity was manually validated by converting X and Y pixel coordinates to timeseries ROIs per movie in Fiji. X and Y pixel coordinates were converted to Euclidian distances in microns to calculate saltation length as validation of the TS phenotype. Pearson's correlation coefficient between soma front and rear was computed using *corrcoef* function in MATLAB.

Calcium imaging

For GCaMP calcium imaging in intact hSSs, hSSs were labeled with AAV-DJ-mDlx-GCaMP6f-Fishell-2 (Addgene, 83899) and placed in a well of a Corning 96-well microplate (Corning, 4580) in NM and imaged using a ×10 objective on a Leica TCS SP8 confocal microscope. GCaMP6 was imaged at a frame rate of 2 Hz. Mean gray values were collected from GCaMP6$^+$ soma with Fiji (ImageJ, version 2.1.0, NIH). Spontaneous calcium transients were detected using a custom-written MATLAB routine (version R2019b, 9.4.0, MathWorks). Mean gray values were transformed to relative changes in fluorescence: $dF/F(t) = (F(t)-F_0)/F_0$, where F_0 represents minimum grey values of the time series of each ROI. Calcium transients were detected as $dF/F(t)$ crossed the threshold of 2 median absolute deviations.

For the GCaMP calcium imaging in hSSs coupled with GABA application, intact hSSs labeled with Dlxi1/2b-mScarlet-P2A-GCaMP6s (Vectorbuilder) were placed in a perfusion chamber (RC-20, Warner instruments) in low-potassium Tyrode's solution (5 mM KCl, 129 mM NaCl, 2 mM $CaCl_2$, 1 mM $MgCl_2$, 30 mM glucose, 25 mM HEPES, pH 7.4). After baseline imaging of mScarlet and GCaMP signals using a 10x objective on a Leica TCS SP8 confocal microscope at the frame rate of 1 frame per second, Tyrode's solution supplemented with 1 mM GABA was perfused. Mean gray values were collected from mScarlet and GCaMP6$^+$ soma with Fiji (ImageJ, version 2.1.0, NIH). GCaMP signal was normalized to mScarlet signal from selected ROIs. Mean gray values were transformed to relative changes in fluorescence: $dF/F(t) = (F(t)-F_0)/F_0$, where F_0 represents the 5th percentile of mean grey values per ROI.

Fura-2 calcium imaging on plated hSS was performed as previously described (Khan et al., 2020). Briefly, cells were loaded with 1 μM Fura-2 acetoxymethyl ester (Invitrogen, F1221) for 30 minutes at 37°C in NM medium, washed with NM medium for 5 minutes and then transferred to a perfusion chamber (RC-20, Warner instruments) in low-potassium Tyrode's solution (5 mM KCl, 129 mM NaCl, 2 mM $CaCl_2$, 1 mM $MgCl_2$, 30 mM glucose, 25 mM HEPES, pH 7.4) on the stage of an inverted fluorescence microscope (Eclipse TE2000U; Nikon). After 0.5 minute of baseline imaging, low-potassium Tyrode's solution supplemented with 100μM GABA was perfused for 1 minute. Imaging was performed at room temperature (~25 °C) on an epifluorescence microscope equipped with an excitation filter wheel and an automated stage. Openlab software (PerkinElmer) and IGOR Pro (version 5.1, WaveMetrics) were used to collect and quantify time-lapse excitation 340 nm/380 nm ratio images, as previously described (Barreto-Chang and Dolmetsch, 2009). Only the cells that had a response higher than 0.1 340 nm/380 nm ratio were included in the analysis.

Calcium imaging for the network activity experiments were performed on intact hCS or hcs assembled with hCS placed on transwells. Prior to assembly, hCS neurons were labeled with AAV-DJ-hSyn1-GCaMP6s (Stanford Gene Vector and Virus Core). GCaMP6 was imaged at a frame rate of 3.8 Hz. Mean gray values were collected from GCaMP6$^+$ soma with Fiji (ImageJ, version 2.1.0, NIH). Mean gray values were transformed to relative changes in fluorescence: $dF/F(t) = (F(t)-F_0)/F_0$, where F_0 represents average grey values of the time series of each ROI. Pairwise correlation coefficients and peak amplitudes were calculated using custom-written MATLAB routines (version R2019b, 9.4.0, MathWorks).

Western blotting

Whole cell protein lysates from hCS and hSS samples from Ctrl and TS hiPSCs were prepared using SDS Buffer (1.5% SDS, 25 mM Tris pH 7.5). Briefly, 75 μL of SDS Buffer was added to two spheres in a 1.5 mL tube. Samples were sonicated for a total of 7-9 seconds using an ultrasonicator (Qsonica Q500 sonicator; pulse: 3 seconds on, 3 seconds off; Amplitude: 20%) using a small tip attachment until samples were no longer viscous. Protein concentrations were quantified using the bicinchoninic Acid (BCA) assay (Pierce,

Thermo Fisher 23225). Protein samples were normalized and prepared in 1X LDS Sample Buffer (NuPAGE LDS Sample Buffer, Thermo Fisher NP007) and 0.1M DTT. Samples (12-15 μg per sample per lane) were loaded and run on a 10%-20% tricine gel (Novex 10%-20% Tricine Protein Gel, Thermo Fisher Scientific), and transferred onto a polyvinylidene fluoride (PVDF) membrane (Immobilon-PSQ, EMD Millipore). Membranes were blocked with 5% BSA (Sigma) in TBST for 1 h at room temperature (RT) and incubated with primary antibodies against β-actin (mouse, 1:50,000, Sigma, A5316), Myosin Light Chain 2 (rabbit, 1:1,000, Cell Signaling, 8505S), and Phospho-Myosin Light Chain 2 (Ser19) (rabbit, Cell Signaling, 1:1,000, 3671S) antibodies for 72 h at 4 °C. Membranes were washed three times with TBST and then incubated with near-infrared fluorophore-conjugated species-specific secondary antibodies: Goat Anti-Mouse IgG Polyclonal Antibody (IRDye 680RD, 1:10,000, LI-COR Biosciences, 926-68070) or Goat Anti-Rabbit IgG Polyclonal Antibody (IRDye 800CW, 1:10,000, LI-COR Biosciences, 926-32211) for 1 hour at RT. Following secondary antibody application, membranes were washed three times with TBST, once with TBS, and then imaged using a LI-COR Odyssey CLx imaging system (LI-COR). Protein band intensities were quantified using Image Studio Lite (LI-COR) with built-in background correction and normalization to β-actin controls.

Whole-cell patch clamping

For patch-clamp recordings, cells were identified as Dlxi1/2b-EGFP$^+$ (hSSs) or hSyn1-eYFP$^+$ (hCSs) with an upright slice scope microscope (Scientifica) equipped with Infinity2 CCD camera and Infinity Capture software (Teledyne Lumenera). Recordings were done with borosilicate glass electrodes with a resistance of 7–10 MΩ. For all experiments, BrainPhys neuronal medium (STEMCELL Technologies, 05790) was used as the external solution. Data were acquired with a MultiClamp 700B Amplifier (Molecular Devices) and a Digidata 1550B Digitizer (Molecular Devices), low-pass filtered at 2 kHz, digitized at 20 kHz and analyzed with pCLAMP software (version 10.6, Molecular Devices). Cells were given a -10mV hyperpolarization (100ms) every 10 s to monitor input resistance and access resistance. Cells were not included for analysis if they had a change > 30%. The liquid junction potential was calculated using JPCalc66, and membrane voltage was manually corrected with an estimated −15-mV liquid junction potential for current clamp recordings.

For calcium current recording, calcium was replaced by barium in the external solutions. Monolayer interneurons at day 140 labeled with Dlxi1/2b-EGFP$^+$were recorded . Cells were held at –70 mV in voltage-clamp and depolarizing voltage steps (500 ms) were given with an increment of 10 mV. The external solution contained 100 mM NaCl, 3 mM KCl, 2 mM $MgCl_2$, 20 mM $BaCl_2$, 25 mM TEA-Cl, 4 mM 4-Aminopyridine, 10 mM HEPES, 20 mM glucose, pH 7.4 with NaOH, 300 mOsm. Internal solution contained 110 mM CsMethylSO_3, 30 mM TEA-Cl, 10 mM EGTA, 4 mM MgATP, 0.3 mM Na_2GTP, 10 mM HEPES, 5 mM QX314-Cl, pH 7.2 with CsOH, 290 mOsm.

For recordings from migrating interneurons, forebrain assembloids were placed on cell culture inserts with 0.4 mm pore size (Corning, 353090). Assembloids on inserts were carefully dislodged and transferred into the recording chamber. Dlxi1/2b-eGFP$^+$ cells migrated into hCS part and near the fusion border of hCS and hSS were recorded. Resting membrane potential was recorded immediately after whole cell. BrainPhys medium was used as the external solution. The internal solution contained 127 mM K-gluconate, 8 mM NaCl, 4 mM MgATP, 0.3 mM Na_2GTP, 10 mM HEPES and 0.6 mM EGTA, pH adjusted to 7.2 with KOH (290 mOsm).

For GABA puffing experiments, plated hSS cells were recorded in BrainPhys neuronal medium in the presence of TTX (1 μM), NQBX (10 μM) and APV (50 μM), with internal solution containing high chloride as follows: 135 mM CsCl, 4 mM MgATP, 0.3 mM Na_2GTP, 10 mM HEPES and 0.6 mM EGTA, pH adjusted to 7.2 (290 mOsm). GABA (100 μM diluted in Brainphys, Tocris, Cat. No. 0344) was filled in a pipette (puffing pipette), placed at a distance of 20 μm away from the soma of the recorded cell, and puffed with different durations (3ms, 5ms, 10ms, 20ms, 50ms, 100ms, 200ms, 500ms) controlled by a picospritzer (General Valve, Picospritzer II). Cells were held at –60 mV under voltage clamp to record GABA-induced inward current. For puff duration of 3 ms, 5 ms, 10 ms, GABA current was recorded once every 10 s, and at least 5 trials were averaged; for puff durations over 20 ms, due to the large responses, cells were recorded at least 2 min after the previous puffing to prevent run down. One Ctrl line and one TS line were recorded on the same day using the same puffing pipette with the same aliquot of GABA to minimize batch bias.

RNA sequencing

RNA was extracted from hSS and hCS using the Quick-RNA Miniprep kit (Zymo Research, R1054). For library construction, non-stranded cDNA libraries were constructed using poly(A) mRNA enrichment and the NEBNext Ultra™ II RNA Library Prep Kit for Illumina following manufacturer's instructions (NEB, E7770S). RNA and library qualities were confirmed using Qubit Flourometric Quantification (Invitrogen, Q33239) and fragment analysis (Agilent). 150bp pair-end sequencing was performed using NovaSeq 6000 Sequencing system (Illumina).

Using STAR (v2.5.2b) (Dobin et al., 2013), reads were mapped to hg38 with the Gencode v25 annotation. Sample identity was verified by descent (IBD) (PLINK v1.09) (Purcell et al., 2007) based on SNPs called from the aligned reads using the GATK Haplotype caller (v3.3) (McKenna et al., 2010). To estimate genetic ancestry, the high-quality SNPs (<5% missing values, minor allele frequency < 0.05, and Hardy–Weinberg equilibrium < 1×10^{-6}) were combined with HapMap3.3 (hg38) and multidimensional scaling (MDS) was calculated. Sample sex was verified by total expression of Y chromosome genes. Regional identity (hCS and hSS) was verified using regional marker genes (hSS: *DLX*, *NKX2-1* and *SLC32A1*; hCS: *SLC17A6*, *SLC17A7*, and *NEUROD2*). The presence of the mutation was verified per individual by combing all reads spanning the mutation locus and identifying the G → A mutation at the chr12: 2504944 locus. Samples with marker genes belonging to different regions higher than two standard deviations from the mean

were removed. Picard sequencing metrics (http://broadinstitute.github.io/picard/, v2.5.0) were summarized using the first 6 principal components (seqPCs) and were included in the model to control for technical variation resulting from the sequencing. Outlier samples (standardized sample network connectivity Z scores < −2) were removed. A total of 94 samples (hCS: 21 Ctrl, 14 TS; hSS: 32 Ctrl, 27 TS) with 17,377 expressed genes (>10 read in 50% of samples) were used for downstream analysis.

For differential expression, gene expression was normalized using the trimmed mean of M values (TMM) method from the edgeR package (Robinson et al., 2010). Differential expression was calculated using the voom method from the limma package. The hiPSC line was used as a blocking factor in the model using the duplicateCorrelation function from the limma package (Ritchie et al., 2015). The model used was ~ Condition + Sex + Differentiation + Sequencing batch + Genetic ancestry MDS1:2 + Age + Reprogramming method + seqPC1:6, where condition was a combination of genotype, region, depolarization and differentiation stage category of cultures (90-129 days). Gene set enrichment analysis (GSEA) was performed on all genes ranked by $\log_2$ fold change using the fgsea package (v1.10.1) (Korotkevich et al., 2021) using with 1,000,000 permutations, a minimal set size of 30 and a maximal set size of 500. Gene ontology (GO) sets (v7.0) were downloaded from http://software.broadinstitute.org/gsea/msigdb/. GO terms with FDR < 0.05 were considered significant.

For plotting gene trajectories, the data were normalized using conditional quantile normalization (cqn v1.3.60) and all covariates used in the differential expression model (except condition) were regressed out. The smoothed line was fitted using the loess method as implemented in ggplot2 (v3.3.3).

For weighted gene network analysis (WGCNA; v1.68) (Langfelder and Horvath, 2008) early stage hSS (40-75 days) hSS data were normalized using conditional quantile normalization (cqn v1.3.60) and the following covariates were regressed out before running the analysis: differentiation stage, region (hCS vs hSS), sex, hiPSC reprogramming method, genetic ancestry MDS1:2 and seqPC1:5.

The following parameters were used for network construction and module selection: soft power = 9, minimal module size = 160, deep split = 4, cut height for creation of modules = 0.9999 and cut height for merging modules of 0.2. The module eigengene (first principal component of the module) was then tested for association with TS using a linear model. Modules were considered associated with TS when FDR < 0.05. For modules associated with TS, biological process and molecular function GO enrichment was performed using cluterProfiler (v3.12.0) (Yu et al., 2012) with default parameters. Modules significantly associated with TS were tested for enrichment for common variation associated with ASD (Grove et al., 2019), SCZ (Pardiñas et al., 2018), ADHD (Demontis et al., 2019), MDD (Howard et al., 2019) and BD (Mullins et al., 2020). SNPs with 10 kb of a gene were assigned to that gene and used. SNP heritability was calculated using a stratified LDscore regression (v1.0.0) (Finucane et al., 2015). Enrichment was calculated as the proportion of SNP heritability accounted for by the genes in the module divided by the proportion of total SNPs within the module. Enrichment for ASD and NDD genes was performed using a Fisher exact test on high confidence gene (gene score < 2 or syndromic genes) from SFARI (https://gene.sfari.org/database/gene-scoring/) or on NDD gene lists from (Leblond et al., 2021). Enrichments with FDR < 0.05 were considered significant.

Statistics

Data are presented as mean ± s.e.m. or boxplots showing maximum, third quartile, median, first quartile and minimum values. RNA sequencing boxplots show center as median, lower hinge as 25% quantile, upper hinge as 75% quantile and whiskers extend to ±1.5× interquartile range. Raw data were tested for normality of distribution, and statistical analyses were performed using paired or unpaired t-tests (two-tailed), multiple t-test with correction for multiple comparisons (Holm- Šídák), Mann–Whitney non-parametric tests and two-way ANOVA tests with Tukey's multiple comparisons. Sample sizes were estimated empirically. MATLAB routines and Fiji macros were used for migration and calcium imaging analysis. GraphPad Prism (version 8.4.2-9.0.0) and MATLAB (version R2019b, 9.4.0, MathWorks) were used for statistical analyses. DaVinci Resolve 16 (Blackmagic Design) was used to generate supplementary videos.